J. Fluid Mech. (2009), *vol.* 622, *pp.* 259–290.
doi:10.1017/S0022112008005156 Printed in the United Kingdom

Direct numerical simulation of the pulsatile flow through an aortic bileaflet mechanical heart valve

M. D. DE TULLIO[1], A. CRISTALLO[1], E. BALARAS[2] AND R. VERZICCO[3]†

[1]DIMeG and CEMeC, Politecnico di Bari, Via Re David 200, 70125 Bari, Italy

[2]Fischell Department of Bioengineering, University of Maryland, College Park, MD 20742, USA

[3]DIM, Università di Roma 'Tor Vergata', Via del Politecnico 1, 00133 Roma, Italy

(Received 27 March 2008 and in revised form 30 October 2008)

This work focuses on the direct numerical simulation of the pulsatile flow through a bileaflet mechanical heart valve under physiological conditions and in a realistic aortic root geometry. The motion of the valve leaflets has been computed from the forces exerted by the fluid on the structure both being considered as a single dynamical system. To this purpose the immersed boundary method, combined with a fluid–structure interaction algorithm, has shown to be an inexpensive and accurate technique for such complex flows. Several complete flow cycles have been simulated in order to collect enough phase-averaged statistics, and the results are in good agreement with experimental data obtained for a similar configuration. The flow analysis, strongly relying on the data accessibility provided by the numerical simulation, shows how some features of the leaflets motion depend on the flow dynamics and that the criteria for the red cell damages caused by the valve need to be formulated using very detailed analysis. In particular, it is shown that the standard Eulerian computation of the Reynolds stresses, usually employed to assess the risk of haemolysis, might not be adequate on several counts: (i) Reynolds stresses are only one part of the solicitation, the other part being the viscous stresses, (ii) the characteristic scales of the two solicitations are very different and the Reynolds stresses act on lengths much larger than the red cells diameter and (iii) the Eulerian zonal assessment of the stresses completely misses the information of time exposure to the solicitation which is a fundamental ingredient for the phenomenon of haemolysis. Accordingly, the trajectories of several fluid particles have been tracked in a Lagrangian way and the pointwise instantaneous viscous stress tensor has been computed along the paths. The tensor has been then reduced to an equivalent scalar using the von Mises criterion, and the blood damage index has been evaluated following Grigioni *et al.* (*Biomech. Model Mechanobiol.*, vol. 4, 2005, p. 249).

1. Introduction

The replacement of heart valves is a safe and routine clinical practice worldwide, adopted whenever the natural valve cannot be restored to its normal function. Since the first successful heart valve replacement four decades ago, more than 50 valve designs have been developed. Bileaflet mechanical heart valves have been used for

† Email address for correspondence: verzicco@poliba.it

over two decades and today remain the most widely implanted valve design due to their durability, good bulk forward flow haemodynamics and a large orifice area which generates small transvalvular pressure drops (see the review by Yoganathan, He & Jones 2004, for a detailed discussion of the literature). Despite their widespread clinical use, however, and the continuous design improvements, mechanical heart valve implants still carry significant risks. In particular, they are still unable to eliminate problems such as haemolysis, platelet activation and thromboembolic events arising from the formation of clots and their subsequent detachment. In fact, red blood cell damage and platelet activation, which eventually leads to thrombosis, can be associated to the augmented mechanical stresses from turbulence, which is generated around and downstream of the valve (Smith *et al.* 1972; Stein & Sabbah 1974). In the studies by Ku & Liepsch (1986), Liepsch (1986) and Liepsch *et al.* (1998), the effects of the mechanical stresses in the blood integrity are analysed taking into account also the non-Newtonian nature of the fluid and the wall elasticity of arteries. When the turbulent eddies are much larger than the blood cell diameter, the former surround the blood cells completely and rotate or translate with the flow without causing much damage. In contrast, when the Kolmogorov scales are similar in size to the blood cells, they directly interact damaging the cell membranes (Liu, Lu & Chu 2000). Prevention of these complications requires lifelong anti-coagulation therapy, inducing high level of haemorrhage risk. On account of the previous arguments, it is clear that there is a need for a better understanding of the valve fluid dynamics especially for what concerns the turbulent flow features in order to assess the valve performance and the subsequent risk of blood damage. Liepsch (1986) arrived at the same conclusion for artificial grafts and vascular surgery.

The development of computational models in the mechanical heart valve field is motivated by medical and economic concerns as well as efficiency. Sufficiently accurate computational models, in fact, would serve as an inexpensive tool for scientific and medical research that, combined with medical imaging and other cardiovascular diagnostic techniques, would provide fundamental information for the improvement in patient care. Despite the progress in numerical methods and the forever increasing power of modern computers, the problem under consideration is still very challenging owing to complex moving geometries, fluid–structure interaction, intrinsic flow unsteadiness and very intense velocity gradients both in space and time. The difficulty stems from the fact that the analysis includes phenomena that are complex problems in their own right: The dynamics of the valve leaflets drives the flow and vice versa, thus implying fluid–structure interaction. The wide disparity in length scales, from the large structures with a scale comparable to the valve orifice (27 mm) up to the flow in the hinge regions (0.1 mm) and even further down to the Kolmogorov scale, requires a very fine spatial resolution over a computational domain long enough to accommodate few of the largest scales. In addition, the important time scales of the flow also vary widely from more than one heart cycle ($\leqslant$1 s) to milliseconds when the valve closes, thus requiring very small time steps and temporal integration for several heart cycles to extract converged phase-averaged statistics. Transition to turbulence and subsequent relaminarization within the same pulsatile cycle also demands sufficiently accurate and non-dissipative numerical methods that will correctly capture the physics of the transitional turbulence without introducing numerical viscosity or other artificial dissipation mechanisms.

In the literature there are several studies dealing with the numerical simulation of the flow in a bileaflet mechanical heart valve, and in most of them one or more

simplifying assumptions are made. Many papers consider the leaflets fixed (Ge *et al.* 2005) or prescribe their motion using simplified kinematics (Yang & Balaras 2006) or kinematics extracted from coordinated experiments (Dasi *et al.* 2007), thus avoiding to cope with the fluid–structure interaction problem. Despite the simplifications made, however, such studies provide useful insights into the complex dynamics of these flows. Dasi *et al.* (2007), for example, provide a very detailed description of the flow vorticity dynamics and comparisons with similar experiments. Other papers dealing with the fluid–structure interaction refer to simplified geometries or two-dimensional flows (Pedrizzetti & Domenichini 2006, 2007). In other studies, only part of the cycle is considered (Myers & Porter 2003) and the numerical simulation imposes symmetries (Cheng, Lai & Chandran 2004) so as to decrease the computational cost. In addition, in the majority of the literature, turbulence models are used to avoid the explicit simulation of the smallest scales (Grigioni *et al.* 2005; Yokoyama *et al.* 2006; Alemu & Bluestein 2007, among many others); this substantially reduces the nodes of the mesh and allows for larger integration time steps, but at the expense of the information on the turbulence fine scales whose accurate description is mandatory for the comprehension of the clinical phenomena mentioned above. Recently, Borazjani *et al.* (2007) and Borazjani, Ge & Sotiropulos (2008) considered the full three-dimensional flow dynamics in an axisymmetric aortic root, including fluid–structure interactions. These investigations clearly demonstrated how important is to consider the complete problem in order to understand the details of the flow physics.

The present paper is an attempt to study the pulsatile flow in a mechanical bileaflet heart valve without making simplifying assumptions on the flow physics and using a realistic aortic root geometry. There are a number of reasons motivating this effort: Many of the phenomena like platelet activation and red blood cell damage are due to high levels of shear stresses produced in the near wake of the valve, and the small-scale turbulence downstream, both of which depend on the way the flow separates at the leaflets. As known from aeronautical applications (dynamic stall), this separation is completely different for steady or moving bodies. Moreover, the valve-closing phase has been implicated with thrombosis initiation owing to intense low-pressure transients which are also responsible for platelet activation. These phenomena can only be captured in a configuration where the valve leaflets dynamically interact with the blood flow. In the present study, we conducted direct numerical simulations (DNS) of the coupled fluid–structure interaction problem. In such case the Navier–Stokes equations are solved without resorting to turbulence models, while the motion of the leaflets and the resulting blood flow is a product of their complex dynamic interaction. The coupled system of equations is integrated for several cardiac cycles, in order to compute converged phase-averaged statistics. The results are compared with analogous experimental data showing very good agreement for both the leaflet dynamics and the mean and r.m.s. velocity profiles downstream, demonstrating the accuracy of the proposed methodology. In terms of exploring the extensive DNS database produced by the above computations, we have focused on understanding the systematic delay in the closing of one of them. In addition, we have tested some of the criteria employed for the evaluation of the red cell damage which compute an equivalent scalar from the Reynolds stress tensor in a Eulerian framework; we have shown that the viscous stress tensor produces comparable effects in different flow regions, and that a Lagrangian tracking of individual trajectories would be needed for a more realistic damage evaluation.

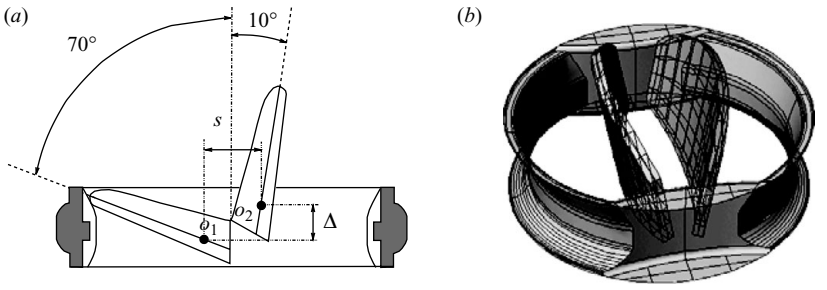

FIGURE 1. (*a*) Range of rotation of the leaflets. (*b*) Geometrical model of the reproduced valve.

2. The problem

2.1. *Numerical set-up*

The valve model considered in the present simulations resembles the 27 mm Bicarbon model by Sorin Biomedica Sorin-Group (2006), which is used in the experiments by Cerroni (2006) and Romano (2008). The two leaflets are symmetric with respect to the valve centreline parallel to the pivot axes and have a curved profile. In this way, a balanced partition of the flow between the central orifice and the lateral ones is obtained. Also, each of the three orifice areas introduces equal resistance to blood flow, with the intent of minimizing turbulence and favouring laminar blood flow on the outflow side. To optimize the organization of the flow, the housing of the valve has an airfoil profile, which gently decreases in width from the inflow towards the outflow side, favouring pressure recovery, guaranteeing surface continuity with the suture ring and minimizing blood stasis close to the patient annulus. A smart hinge design based on the coupling between two spherical surfaces with different radii of curvature (leaflet pivot and hinge recess) allows the leaflets to rotate virtually without sliding between the pivot and the slot within the housing. This introduces a small axial translation Δ of the leaflets and a smaller variation of their relative distance s (figure 1*a*). The friction to rotation is minimized and an uninterrupted washing of the exposed surfaces is allowed.

In our numerical simulations, the geometry of the valve closely mimics the real model (see figure 1*b*) except for the microscopic hinge mechanism that is not included. Instead, we introduced a small gap in the hinge regions to mimic the continuous washing through the effluent chimneys of the real mechanism. We allowed the leaflets also for an axial translation in addition to rotation and, for the present combination of valve model and aortic root geometry, this feature was necessary to obtain a satisfactory agreement with the experiments (see § 3.2). The friction in the hinges is neglected, since reliable data are not available and it should be anyway much smaller than the moment produced by the flow. Our hinge gap size (340 μm) is larger than that of the real valves ($\leqslant$250 μm), and this choice was necessary to alleviate computational problems, like high backflow velocities when the valve was closed, and adequate spatial resolution (six to seven nodes on the cross-stream direction of the gap, in a grid with 6.6 million nodes). As shown in figure 1(*a*), the rotation arc of each leaflet during the motion is fixed to 60°: this means that each leaflet starts from an angle of 10° with respect to the streamwise direction (fully open position) and stops at an angle of 70° (fully closed position). It is worth noting that in the numerical simulations, the actual fully closed position is limited to an angle of 68° with respect to the streamwise direction: a small gap is always left between the leaflets and the

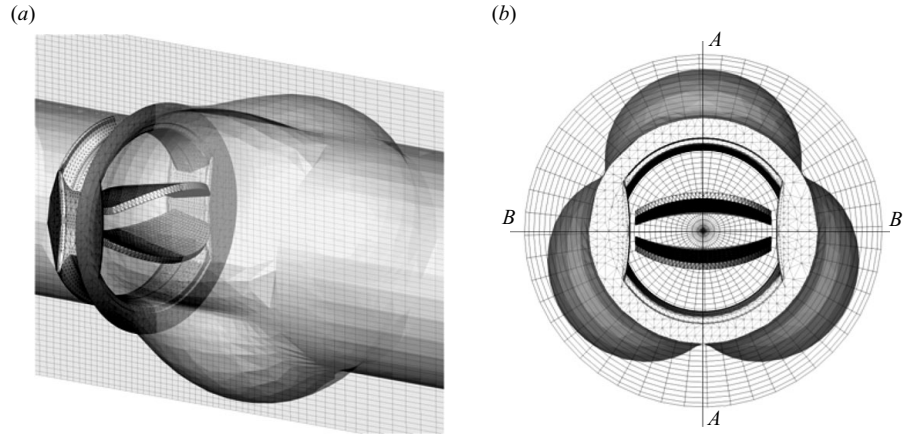

FIGURE 2. Computational grid (only one in every four grid lines is plotted) around modelled valve. The aortic root, the surfaces of valve housing and two leaflets are discretized using triangular meshes (Stereo Lithography Format). In (*b*), the traces of the planes AA and BB over which the flow is mainly analysed are reported.

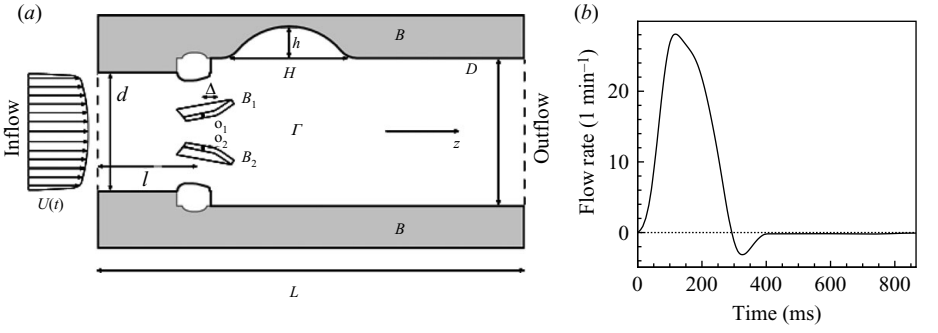

FIGURE 3. (*a*) Sketch of the valve/aortic root arrangement with the main lengths of the problem. Main lengths: $D = 1.26d$, $l = d$, $L = 5d$, $H = 1.14d$, $h = 0.26d$. (*b*) Time evolution during one cycle of the aortic flow rate.

housing in order to allow some backflow when the valve is closed and to avoid very high values of the velocity in the quasi-closed configuration where cavitation might become an issue.

The geometry of the aortic root exactly reproduces the model used for the experimental investigations of Cerroni (2006) and Romano (2008) and closely corresponds to the physiological case: at the outlet of the valve, the three sinuses of Valsalva are placed at equispaced radial positions (see figure 2). The valve is mounted in an *intra-annular* configuration, meaning that the valve housing does not extend into the sinuses of Valsalva, and in an asymmetric orientation with respect to the sinuses (figure 2*b*). A sketch of the valve/aortic root arrangement is given in figure 3(*a*), together with the main dimensions of the problem. The inflow velocity profile is assigned by a hyperbolic tangent function with stretching parameter $\gamma = 60$, which yields a flat velocity distribution in the bulk and accommodates the no-slip boundary condition at the aortic wall within a layer of thickness $\lambda/d = 1/\sqrt{Re} \simeq 1.2 \times 10^{-2}$. This velocity profile is modulated in time to mimic the physiological flow rate produced

by the heart in the left ventricle (figure 3*b*), which was used in the experiments by Cerroni (2006) and Romano (2008). The cycle duration was set at 866 ms, corresponding to about 70 beats min^{-1} (natural heart rate at rest). The mean flow rate was adjusted to about 5 $\mathrm{l\,min}^{-1}$ with a peak flow rate of about 28 $\mathrm{l\,min}^{-1}$. It is important to note the presence of a small leakage flow in the second part of the cycle ($t > 400$ ms), which is typical of bileaflet mechanical heart valves, occurring from the hinges gaps. These are typical physiological conditions under an adult aortic valve operates. It is worth mentioning that the present configuration, which consists of a Sorin Biomedical bileaflet mechanical valve and a physiological aortic root with three Valsalva sinuses, has been chosen because of the availability of detailed experimental measurements that will be used for validation. In clinical practice, however, sometimes the sinuses are sacrificed to produce an axisymmetric cylindrical aortic root (Bental procedure), indicating that axisymmetric geometries should also be considered for completeness.

Let B be the aortic root and the valve housing both rigid and fixed in space, while B_1 and B_2 are the two valve leaflets which can rotate about their own pivots o_1 and o_2, which in turn can axially translate within a range Δ. If Γ is the time-dependent fluid domain, the governing equations read

$$\frac{\partial \boldsymbol{u}}{\partial t} + \boldsymbol{\nabla}\cdot(\boldsymbol{u}\boldsymbol{u}) = -\boldsymbol{\nabla} p + \frac{1}{Re}\boldsymbol{\nabla}^2\boldsymbol{u} + \boldsymbol{f}, \tag{2.1}$$

$$\boldsymbol{\nabla}\cdot\boldsymbol{u} = 0, \qquad \text{on } \Gamma$$

$$I_i \frac{\mathrm{d}^2\theta_i}{\mathrm{d}t^2} = T_i, \qquad M_i \frac{\mathrm{d}^2 z_i}{\mathrm{d}t^2} = F_i \qquad \text{for } B_i \quad \text{with} \quad i = 1, 2. \tag{2.2}$$

Equations (2.1) are the Navier–Stokes equations for an incompressible viscous Newtonian fluid and they determine the flow whose velocity vector is $\boldsymbol{u}$, p is the pressure, $\boldsymbol{f}$ is the direct forcing of the immersed boundary method (Fadlun *et al.* 2000) and Re is the Reynolds number later specified. The fluid model is Newtonian, since the blood in large arteries behaves accordingly (Nichols & O'Rourke 1990). The whole blood may be regarded, from a mechanical point of view, as consisting of flexible red cells suspended in a Newtonian fluid, the plasma (Caro *et al.* 1978). When the characteristic length of the problem becomes comparable with the size of red cells, their flexibility plays an important role in determining the viscosity (rouleaux, which are stacks of blood cells, are known to form at low shear rates), and this leads to a non-Newtonian behaviour under specific conditions. Several studies with human blood (Whitmore 1968) have shown the variation of the effective viscosity (the ratio of measured viscous stress to the rate of strain in a laboratory viscometer) with the shear rate. When the latter is about 100–1000 s^{-1} (depending on the hematocrit level), which is typical for many blood vessels *in vivo*, the non-Newtonian behaviour becomes irrelevant and the effective viscosity approaches an asymptotic value. Only with the reduction of the shear rate, the effective viscosity starts increasing, until for a shear rate smaller than 1 s^{-1} it rises extremely steeply; such small values, however, are characteristic of the slow flows in capillaries, whose diameter can be even smaller than that of a red cell, and are not relevant to our study.

Equations (2.2) describe the motion of the leaflets through their angular and axial positions by the dimensionless moments of inertia I_i about the pivots and the masses M_i, T_i and F_i are, respectively, the tilting moments about the pivots and the axial forces resulting from the viscous stress tensor $\boldsymbol{\tau}$, and the pressure integrated over the

leaflets surfaces S_i. Their specific expressions are

$$T_i = \int_{S_i} [(\boldsymbol{\tau} \cdot \boldsymbol{n} - p\boldsymbol{n}) \times \boldsymbol{r}] \cdot \hat{\boldsymbol{x}} \, \mathrm{d}S \quad \text{and} \quad F_i = \int_{S_i} (\boldsymbol{\tau} \cdot \boldsymbol{n} - p\boldsymbol{n}) \cdot \hat{\boldsymbol{z}} \, \mathrm{d}S \quad i = 1, 2, \tag{2.3}$$

with $\boldsymbol{n}$ the outer normal to the surface S_i of the ith leaflet, $\boldsymbol{r}$ the vector given by the distance from the pivot axis to the surface element $\mathrm{d}S$, $\hat{\boldsymbol{x}}$ the unit vector aligned with the pivot axis and $\hat{\boldsymbol{z}}$ its axial counterpart. It is worth mentioning that T_i and F_i depend explicitly on p and $\boldsymbol{u}$, the latter through $\boldsymbol{\tau}$, but implicitly also on θ_j, $\mathrm{d}\theta_j/\mathrm{d}t$, z_j and $\mathrm{d}z_j/\mathrm{d}t$ for $j = 1, 2$ which determine the position in space of the leaflets, the domain Γ and the boundary conditions on the immersed boundaries, and therefore the forcings $\boldsymbol{f}$ in (2.1). We wish to stress that the computation of forces and moments through (2.3) might present accuracy problems in the immersed boundary context, since the leaflet surfaces are not coordinate surfaces and quantities need to be interpolated. Nevertheless, we will show in §§ 2.2 and 3.1 that the results are largely independent of the mesh size and agree very well with similar experiments, thus confirming the reliability of the method.

The incompressible Navier–Stokes equations are discretized in space using second-order-accurate central differences in conservative form and in cylindrical coordinates. The resulting system is inverted using a fractional-step method, where the viscous terms are computed implicitly and the convective terms explicitly. The large-banded matrix associated with the elliptic equation is reduced to a penta-diagonal matrix using trigonometric expansions (FFTs) in the azimuthal direction, and the resulting Helmholtz equations are then inverted using the FISHPACK package (Swartzrauber 1974). A hybrid low-storage third-order Runge–Kutta scheme is used to advance the equations in time; this procedure has the advantage of requiring only a two-level storage, like common second-order schemes, while benefiting from an increased stability limit and a smaller discretization error. All the simulations have been run with a fixed Courant number $CFL = 0.25$, thus having a variable time step Δt which is adjusted accordingly (figure 4*a*); the use of a non-uniform Δt did not affect the time accuracy of the method, since the third-order Runge–Kutta is a 'self-starting' integration scheme which does not need information from the previous times to advance a new Δt. There is an evident computational advantage in the use of a variable time step for the integration of the present flow; in fact, it will be shown in the following sections that the opening and closing of the leaflets are extremely fast events that need small time steps to be accurately simulated even if they occupy only about 20 % of the cycle. On the other hand, for more than 50 % of the cycle the mean flow is essentially zero, the valve leaflets remain still and the flow can be integrated with much larger time steps.

More details on the Navier–Stokes solver are given in Verzicco & Orlandi (1996) and Fadlun *et al.* (2000).

The immersed boundary technique used in this work is based on that proposed in Fadlun *et al.* (2000) and Iaccarino & Verzicco (2003) and extended in Cristallo & Verzicco (2006) for fluid–structure interaction problems; in the latter reference, details of the procedure can be found, together with benchmarks and validation checks. It is worth noting that, in the immersed boundary framework, the motion of the leaflets requires the use of the geometrical preprocessor at each time step, in order to tag the new position of the computational cells with respect to the body: this overhead is about the 20 % of the total computational time. The procedure is more accurate and less expensive than a standard body-fitted approach where, due to the large leaflet motions, it is difficult to adapt the fluid mesh maintaining a proper quality, and the

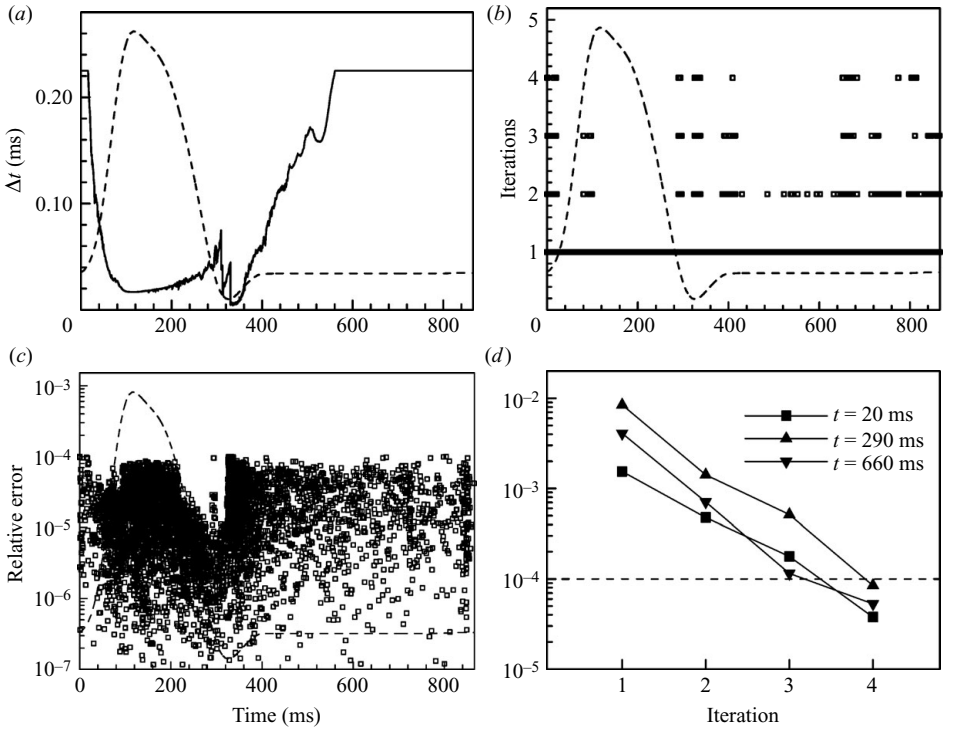

FIGURE 4. Time-step size (*a*), number of FSI iterations (*b*) and relative error (*c*) during a cardiac cycle. (*d*) Convergence history corresponding to three instants of the cycle with four iterations. In panels (*a*)–(*c*) the curve of the flow rate (in arbitrary units) is reported by a dashed (– – – –) line.

change in topology during remeshing requires interpolation techniques; this not only introduces artificial diffusivity, but is also very time-consuming, especially for complex three-dimensional problems.

A strong coupling scheme is employed for the solution of the system (2.1)–(2.2) where the fluid and the structure are treated as elements of a single dynamical system, and all governing equations are integrated simultaneously in the time domain. This complication arises from the fact that the prediction of the flow field and of the hydrodynamic loads requires the knowledge of the motion of the structure and vice versa. For this reason, Hamming's fourth-order predictor–corrector method as described in Yang, Preidikman & Balaras (2008) is used to integrate (2.2) through an iterative scheme until convergence is achieved. More in detail, (2.2) are expanded to a system of first-order ordinary differential equations in the variables θ_i, $\dot{\theta}_i$, z_i and $\dot{z}_i$ with the generalized loads on the right-hand side L_{ij}, $i = 1, 2$ and $j = 1, 4$. The fluid solver is then coupled with the structural solver as follows: (*a*) find the predicted location and velocity of the body using (2.2), with forces and moments computed from $\boldsymbol{u}$ and p at the previous time step; (*b*) find the predicted fluid velocity and pressure fields using (2.1), with the boundary conditions provided by step (*a*), and compute the new resulting loads on the structure through (2.3); (*c*) compute the corrected location and velocity of the body using (2.2); (*d*) check for convergence that we assessed with the leaflets angular velocity, since it was the most sensitive quantity. If $e_j = |^c\dot{\theta}_j - ^p\dot{\theta}_j|$, $j = 1, 2$ is greater than the prescribed tolerance ϵ, repeat steps (*b*)

to (d) and check again convergence with the predicted angular velocity updated as ${}^{p}\dot{\theta}_j = {}^{c}\dot{\theta}_j$, and the new corrected angular velocity ${}^{c}\dot{\theta}_j$ recomputed from (2.2) (the same operations are also performed on θ_i, z_i and $\dot{z}_i$). If convergence is achieved, find the final fluid pressure and velocity fields from the Navier–Stokes equations. In all our computations, a tolerance of $\epsilon = 10^{-4}$ was used. The number of iterations required for convergence at each time step varied from 1 to 4, depending on the phase of the dynamics (see figure 4*b*); convergence is typically more difficult during the opening and closing phases when the leaflets rotate (and translate) very rapidly, while the criterion is satisfied already at the first iteration when the leaflets remain still or move slowly.

As noted by Borazjani *et al.* (2008), the very low moment of inertia of the valve leaflets, owing to the added mass effect, induces numerical instabilities in the fluid–structure interaction algorithm that compromises its stability and prevents it from converging. Le Tallec & Mouro (2001), Causin, Gerbeau & Nobile (2005) and Borazjani *et al.* (2008) suggested that an under-relaxation of the generalized loads is necessary for the solution of the structural part, and the same strategy has been indeed adopted also in the present study by using the expression $L_{ij} = \gamma L^{l}_{ij} + (1-\gamma)L^{l-1}_{ij}$ with $\gamma = 0.9$, l the actual iteration level and $l-1$ the previous one. We wish to point out that, unlike Borazjani *et al.* (2008) in which the under-relaxation parameter γ was dynamically computed during the simulation, in the present study, γ was maintained fixed in time and its value has been chosen by a trial-and-error process using preliminary coarse numerical simulation. Nevertheless, although the value of γ might not be optimal, the convergence of the fluid structure interaction scheme was always achieved with an error below the prescribed tolerance (figure 4). We conjecture that part of the robustness of the method is due to the adaptive time step that automatically reduces its amplitude when the leaflets rotate rapidly (figure 4*a*); this yields a starting error, in the predictor step of the fluid–structure interaction procedure, which is more or less constant during the flow cycle and which is decreased below the tolerance ϵ by a limited number of iterations (figure 4*d*).

As a partial confirmation of the above argument, we note that the third-order Runge–Kutta scheme has a theoretical stability limit of $CFL = \sqrt{3}$ that, with the help of the viscous terms, can be extended up to $CFL \simeq 2$. Nevertheless, we have run our simulations using $CFL = 0.25$, since we have noted that larger stability parameters while increasing proportionally the time step size also increased the initial error of the fluid–structure interaction algorithm that needed more iterations to converge; this resulted in an overall increase of the CPU time.

2.2. *Flow parameters and simulation grid independence*

We have assumed as main scaling quantities the inflow diameter $d = 27\,\mathrm{mm}$ and the bulk velocity at the peak inflow $U = 0.81\,\mathrm{m\,s^{-1}}$ which with a blood kinematic viscosity $\nu = 3.04 \times 10^{-6}\ \mathrm{m^2\,s^{-1}}$ yield a Reynolds number $Re = Ud/\nu = 7200$. The basic time unit is given by $t_b = d/U = 33.3\,\mathrm{ms}$, so that the heart cycle of 866 ms turns out to be $\mathscr{T} \simeq 26 t_b$. Concerning the leaflets made of pyrolytic carbon, with density of $\rho_l = 2000\ \mathrm{kg\,m^{-3}}$, whereas the blood density is $\rho_b = 1060\ \mathrm{kg\,m^{-3}}$. In dimensional units, each leaflet has a mass of $4.086 \times 10^{-4}\,\mathrm{kg}$ and a moment of inertia with respect to the pivot axis of $7.947 \times 10^{-9}\ \mathrm{kg\,m^2}$ that when scaled, respectively, with $\rho_b d^3$ and $\rho_b d^5$ become $M_i = 2.076 \times 10^{-2}$ and $I_i = 2.77 \times 10^{-4}$, $i = 1, 2$ used in (2.2). Additional details of the computational set-up are given in figure 3(*a*) and in its caption where the values are reported.

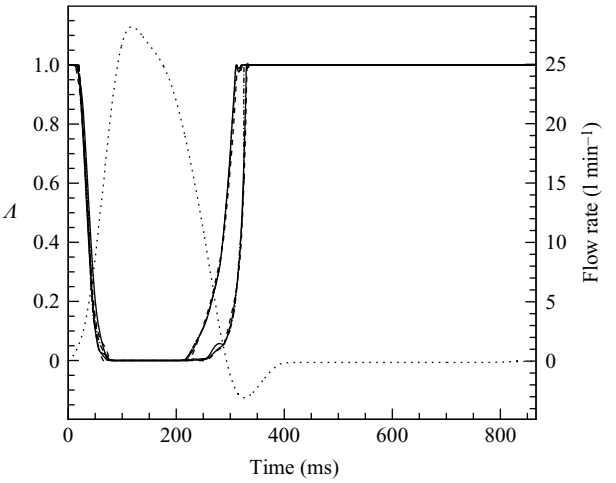

FIGURE 5. Leaflets kinematics for the coarse (– – – –), fine (———) and finest (— · —) grids. The variable Λ is defined as $\Lambda = (\alpha_{open} - \alpha)/(\alpha_{open} - \alpha_{closed})$. The flow rate is reported by a dotted (·····) line.

The aortic root, the valve housing and the leaflets are discretized with unstructured triangular meshes (Stereo Lithography Format, STL) and are embedded into the background cylindrical structured grid. Three computational grids are used, in order to test the grid independence of the results. The coarse mesh employs $129 \times 103 \times 189$ nodes, the fine grid $193 \times 137 \times 250$ nodes, while the finest has $251 \times 147 \times 322$ nodes in the azimuthal, radial and axial directions, with about 2.5, 6.6 and 11.9 million points, respectively. Figure 2(a, b) shows the fine grid, where only one in every four grid lines is plotted. All the grids are clustered near the valve, where rich vorticity dynamics is observed.

Except for the finest grid that was used only for evaluating grid independence and was advanced for three periods, 10 cardiac cycles are computed for all other cases. Each cycle is discretized by a variable time step ranging from $\Delta t_{min} = 10^{-4} t_b$ (about 3 μs), occurring at the flow rate peak and when the valve closes, to a maximum value of $\Delta t_{max} = 7.5 \times 10^{-3} t_b$, (about 250 μs) during the diastole. It is worth noting that the numerical temporal resolution is very high compared to the time interval between two subsequent frames used in the PIV measurements of Cerroni (2006) that varied from 400 up to 3000 μs. The CPU time for the computation of each complete cycle on the fine mesh was about 60 h on a single P-IV processor, equipped with 1 Gb of RAM.

First, the ensemble-averaged flow features of the numerical simulations on the different grids are compared, in order to show grid independence of the averaged results. In particular, figure 5 shows the phase-averaged angular position of the leaflets, and figure 6 the mean and r.m.s. streamwise velocity profiles in the plane AA at a distance of 5.41 mm for three different representative times during the cycle. The leaflet kinematics are identical on all grids. The same applies to the mean velocities for the two finer grids. Note that in figure 6 the r.m.s. velocity profiles for the finest grid are not included due to the limited statistical sample. The comparison of the other two grids is however very satisfactory, and the same kind of agreement is obtained for other quantities or sections. Finally in figure 7 also, the azimuthal (out-of-plane) vorticity contours for the same instants as figure 6 are reported for the fine and

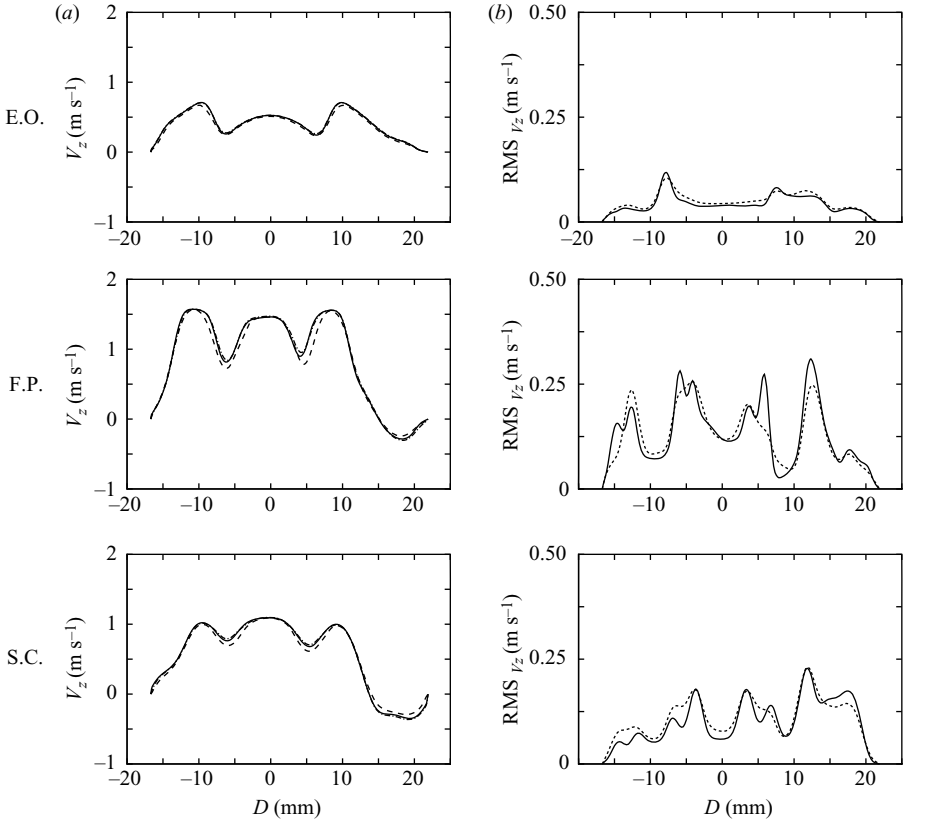

FIGURE 6. Phase-averaged streamwise velocity profiles (*a*) and r.m.s. (*b*) in the symmetry plane AA (in m s^{-1}) at a distance equal to 5.41 mm from the fully open leaflets' tip for the coarse (– – – –), fine (———) and finest (— · —) grids. The r.m.s. velocity profile is missing for the finest grid because that simulation has not been advanced in time long enough to get converged statistics.

finest grids, showing that not only the velocity and its statistics are grid-independent, but also the velocity gradients. Hereafter, in the discussion of the results and in the comparison of the experiments, only the data obtained on the intermediate mesh will be used.

3. Results

3.1. *Data validation*

As a first step, the numerical results have been validated by a comparison with an experiment performed at the University of Roma 'La Sapienza' in the context of the SMART-PIV IST-2002-37548 European Project by the group of Professor G. P. Romano (Romano 2008). All the problem details, from the valve model to the geometry of the aortic root and the flow conditions, have been set in the numerical simulation in order to replicate, as close as possible, the experimental conditions. In figure 8, the time evolution of the leaflets angular position is shown, together with the aortic flow rate for reference. It should be mentioned that the data refer to phase-averaged values since, although small, cycle-to-cycle differences are present. The experimental results are extracted from a high-speed camera recording (at 1000 fps)

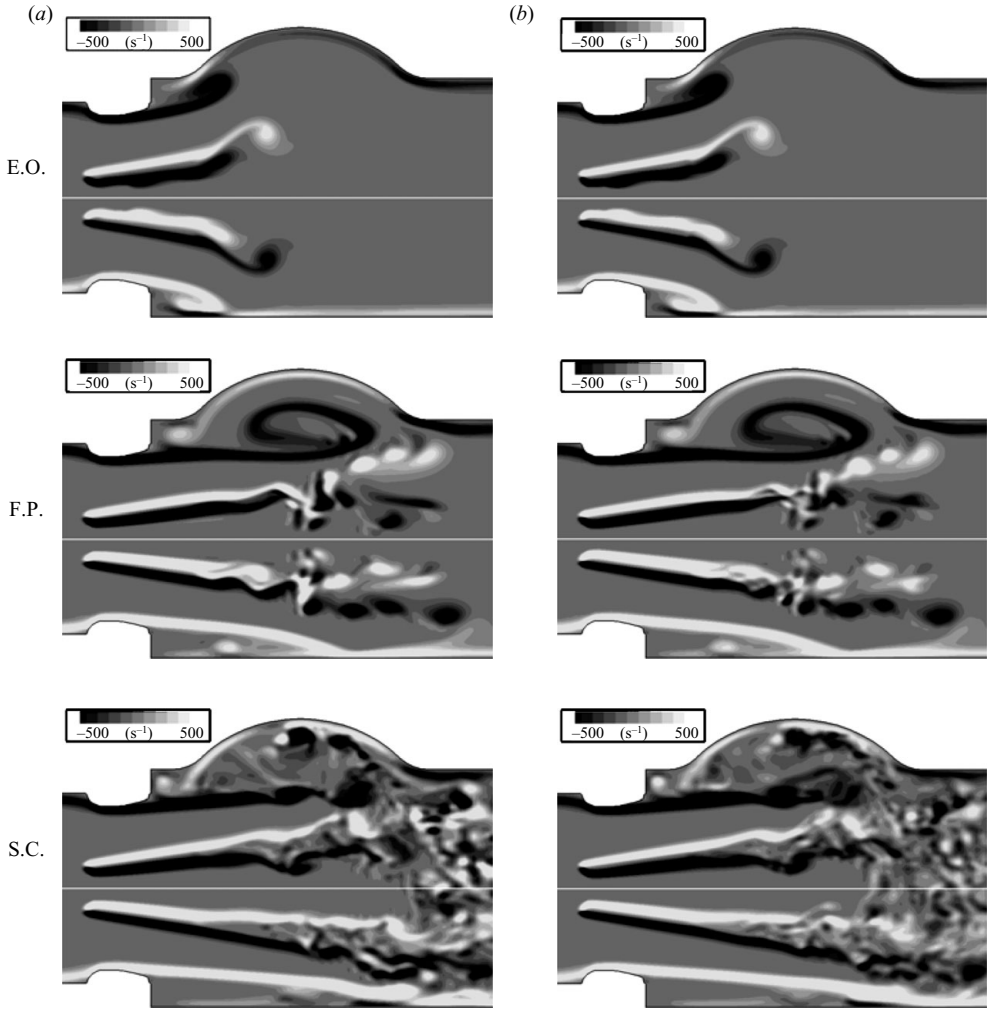

FIGURE 7. Instantaneous vorticity contours in the symmetry plane AA (in s^{-1}) for the fine (*a*) and finest (*b*) grids. Vorticity ranges from $-500\,s^{-1}$ to $500\,s^{-1}$.

of about 10 cycles. It is observed that the main dynamics is well reproduced by the numerical simulation both in the opening and closing phases. In the latter, in particular, a time delay in the closing of one of the leaflets is evident (the upper half in figure 2*b*), and it is of the order of 20 ms. This is a result of the asymmetric mounting of the valve with respect to the Valsalva sinuses (figure 2*b*) and will be discussed more in detail in a successive section. As a further confirmation of the above statement, it is worth mentioning that in the paper by Borazjani *et al.* (2008), in which the aortic root is axisymmetric, the opening and closing dynamics of the leaflets is perfectly synchronous, apart from the minor differences induced by the three-dimensional nature of the flow.

Some instantaneous snapshots of the experimental results are given in figure 9 where the asynchronous closing of the leaflets is also evident. In figure 9(*d*), we show a comparison of the position of the right leaflet with that in the fully open configuration of figure 9(*c*), which is indicated with a dashed line. Although the tilting

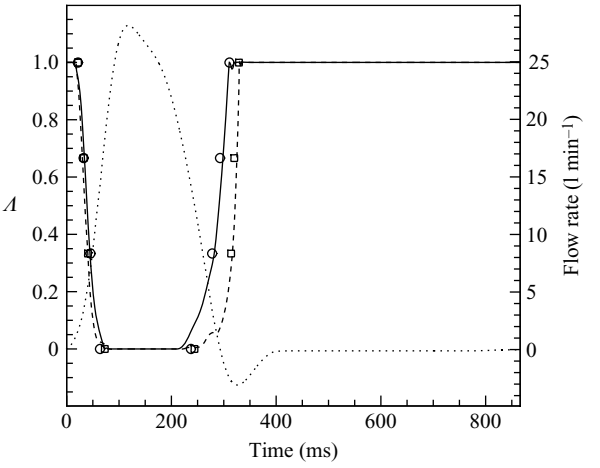

FIGURE 8. Time variation of the phase-averaged leaflets angular position $\Lambda = (\alpha_{open} - \alpha)/(\alpha_{open} - \alpha_{closed})$ and flow rate (·····): comparison with experimental results (symbols) of Cerroni (2006); – – – – □ for leaflet 1 of figure 3, ——— and ○ for leaflet 2.

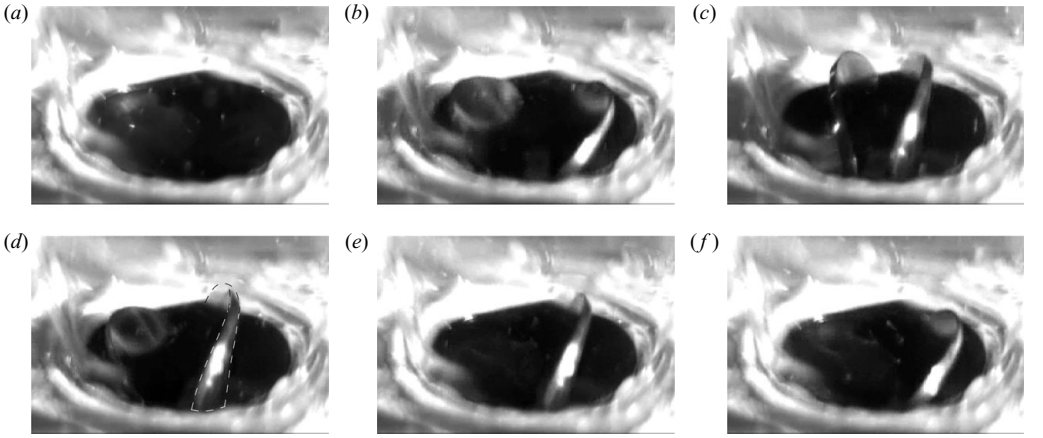

FIGURE 9. Instantaneous snapshots of the valve leaflets dynamics from an experimental visualization: (*a*) $t \simeq 0$ ms, (*b*) $t \simeq 30$ ms, (*c*) $t \simeq 60$ ms, (*d*) $t \simeq 250$ ms, (*e*) $t \simeq 310$ ms, (*f*) $t \simeq 340$ ms. Courtesy of G. P. Romano, reproduced with permission.

angle does not change appreciably, there is a backward axial translation, allowed by the hinge mechanism, which turned out to be very important in the closing delay and that will be investigated in the next section.

Figures 10 and 11 show the phase-averaged streamwise velocity profiles with their r.m.s. fluctuations at different times (start opening, SO; end opening, EO; flow rate peak, FP; start closing, SC; end closing, EC) in the symmetry plane (AA in figure 2*b*) in two sections downstream of the valve, at a distance equal to 5.4 and 23.3 mm from the fully open leaflets' tip, respectively. Also in this case, the agreement with the experiments is generally good, although there are some small discrepancies that are probably due to the limited statistical sample in the simulations. In particular, statistics for the DNS were accumulated over 10 pulsatile cycles, while the experiments were ensemble-averaged for over 200 cycles; considering the intrinsic flow unsteadiness and

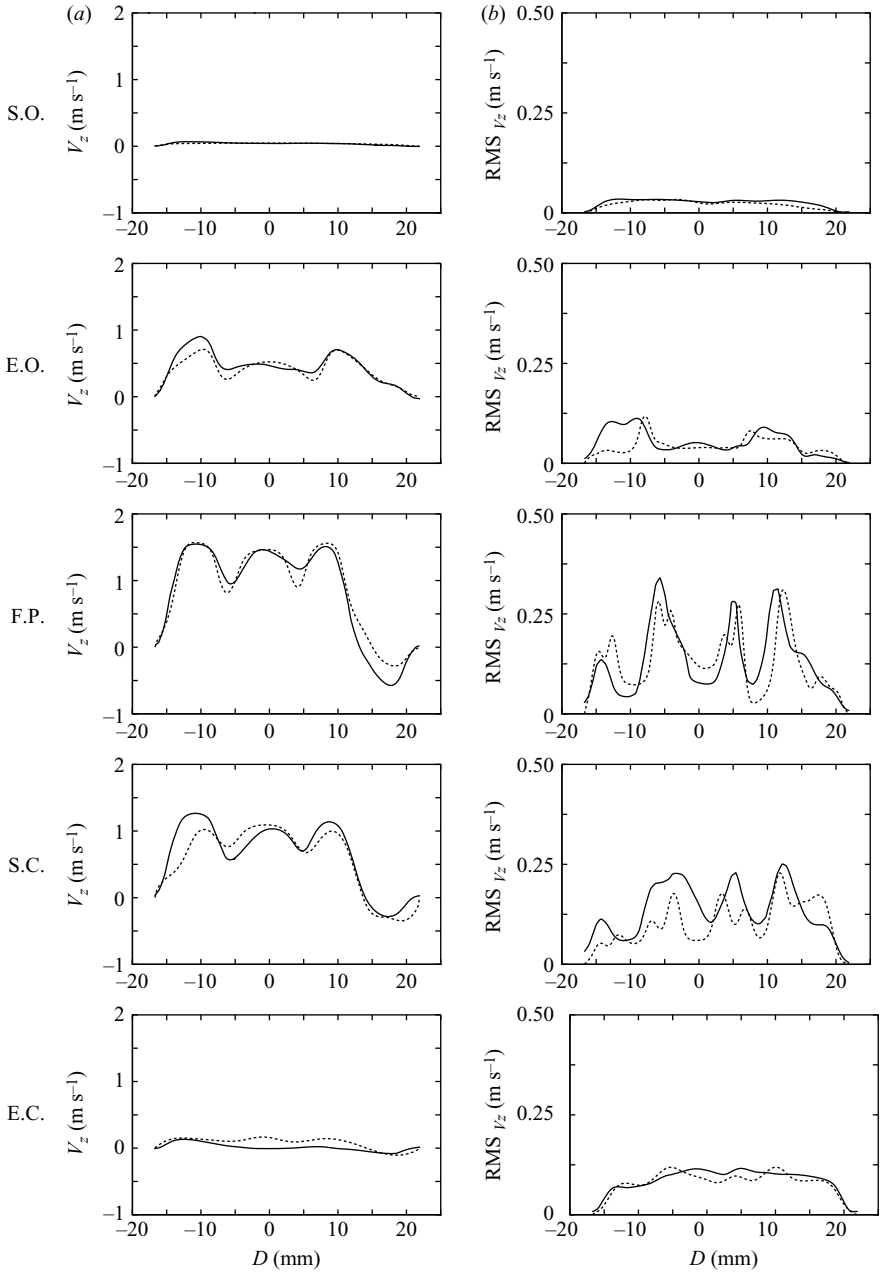

FIGURE 10. Phase-averaged streamwise velocity profiles (*a*) and r.m.s. (*b*) in the symmetry plane AA (in m s^{-1}) at a distance equal to 5.41 mm from the fully open leaflets' tip. ———: experimental results of Cerroni (2006); – – – –: present numerical results (SO: start opening; EO: end opening; FP: flow rate peak; SC: start closing; EC: end closing).

the cycle-to-cycle variations, this can account for some of the differences, especially in the r.m.s. profiles that need more samples to converge. We should also note that, during the accelerating systolic phase the flow remains essentially laminar and repeatable from cycle to cycle (see also Dasi *et al.* 2007), and therefore the averaged

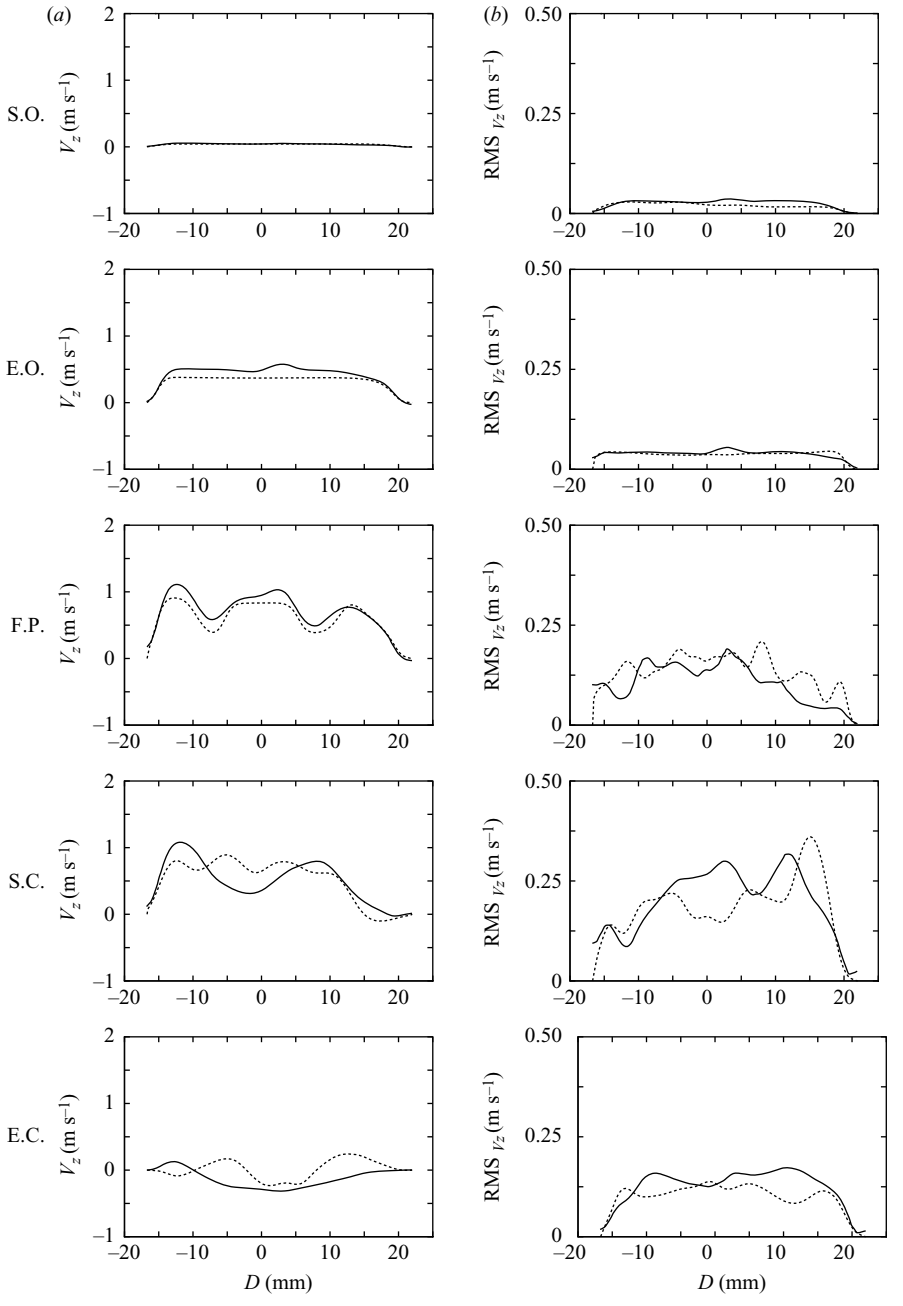

FIGURE 11. Phase-averaged streamwise velocity profiles (*a*) and r.m.s. (*b*) in the symmetry plane AA (in m s^{-1}) at a distance equal to 23.3 mm from the fully open leaflets' tip. ———: experimental results of Cerroni (2006); – – – –: present numerical results (SO: start opening; EO: end opening; FP: flow rate peak; SC: start closing; EC: end closing).

and r.m.s. fields should statistically converge more rapidly. This is evident from figures 10 and 11 where the comparison with experiments is generally better for the SO, EO and FP instants than for the SC and EC times, the last two being in the decelerating part of the flow rate.

In PIV measurements, to eliminate localized errors in the velocity vectors, it is a common practice to correct the raw acquired data with a smoothing filter; in the present experimental results, this was achieved by a 3×3 point averaging in which each vector was averaged with the in-plane eight surrounding vectors. In order to allow a close comparison between numerical simulation and experiments, we have adopted a similar procedure on the former results indeed obtaining a better agreement. We wish to stress, however, that the filtering in the two cases is not exactly the same owing to the different uniform spatial resolution of the experimental PIV data and the non-uniform mesh in the numerical simulations. Finally in the experimental set-up, image distortions in the flow region corresponding to the sinuses of Valsalva were present due to imperfect refractive index matching between the fluid (aqueous glycerin–water solution, 40 % glycerin) and the model (transparent Plexiglas). These distortions might produce localized alterations of the amplitude and shape of the velocity profiles and derived quantities. In Brücker *et al.* (2002), a similar problem was mentioned and an *ad hoc* correction was conducted by mapping the distorted image of a square test grid back to its original shape. In our reference experimental data, this correction was not applied to avoid additional complications (G.P. Romano, personal communication).

As an aside we also note that in the PIV measurements there is a different time interval between two subsequent frames, that varied from 400 up to 3000 μs and from which the velocity field is computed, with respect to the numerical simulation whose time step size was in between 3 and 250 μs; this is another difference that should be kept in mind when comparing the results.

3.2. *Leaflets dynamics*

As already mentioned, the hinge mechanism of the valve yields very complex kinematics, since each pivot is independent of the other and each leaflet is allowed to translate and rotate about an axis which is not fixed in space. In the computations, we initially considered the simplest configuration by assuming that the leaflets could only rotate about fixed axes, whose position was symmetric about a central plane, and the results were only partially in agreement with the experiments. Looking more carefully at the experimental results, we noticed that the leaflets also had an appreciable translation in a direction mostly parallel to the main fluid motion; thus, in the second set of simulations, we have given the leaflets the possibility to axially translate within a given range. As shown in figure 12, this addition was important in matching the experimental results especially in the final part of the closing phase. It is worth mentioning that, in contrast to the present study, the results of Borazjani *et al.* (2008) show that in their case the axial translation of the leaflets is not an essential feature to obtain a good agreement with the experiments. On one hand, it suggests that this might be an issue mainly related to the specific combination of the present heart valve design with the geometry of the aortic root, nevertheless it also evidences the extreme sensitivity of the flow to small kinematic or geometric details of the problem which therefore cannot be disregarded *a priori*.

Looking at figure 12, the leaflets dynamics can be summarized as follows: The opening phase (SO) starts at the beginning of the systole when the flow starts accelerating, and ends before the conclusion of the flow acceleration by reaching the fully open position (EO). The leaflets remain fully open during the peak of the flow rate curve (FP). The closing phase (SC) starts only at the beginning of the steepest flow deceleration and ends at the minimum (negative) of the flow rate by reaching the fully closed position (EC). From figure 12 it is evident that the valve is already fully

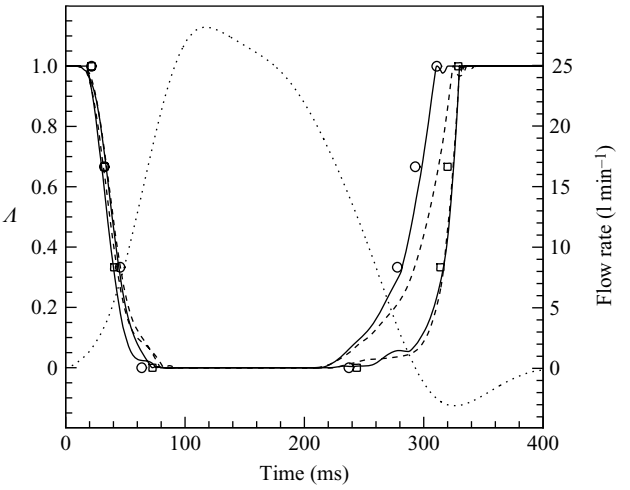

FIGURE 12. Time variation of the phase-averaged leaflets angular position $\Lambda = (\alpha_{open} - \alpha)/(\alpha_{open} - \alpha_{closed})$ and flow rate (·····) for the valve with axial displacement (———) and without axial displacement (– – – –). Symbols: experimental results of Cerroni (2006).

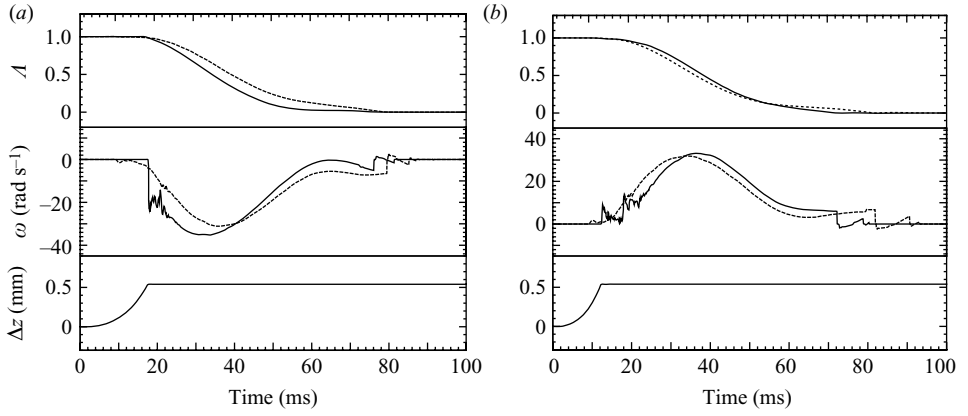

FIGURE 13. Opening phase: time variation (in ms) of the phase-averaged leaflets' angular position $\Lambda = (\alpha_{open} - \alpha)/(\alpha_{open} - \alpha_{closed})$ (top), angular velocity (middle) and axial displacement (bottom). (*a*) Leaflet 1, (*b*) leaflet 2. (———) valve with axial displacement and (·····) without axial displacement.

open when the flow rate reaches about three-fourth of the peak value, and it maintains this configuration for slightly less than 20 % of the pulsating period T. The opening phase of the valve lasts about 8 % of T, while closing lasts approximately 14 % of T, and strongly depends on the temporal variation of the flow rate. In particular, the closing time depends on how steep is the flow-rate decrease, since it is related to the adverse pressure gradient that, in turn, determines the leaflets angular acceleration. It is worth mentioning that from preliminary simulations we have observed the opening of the leaflets to have little sensitivity to the waveform of the flow-rate increase while, in contrast, the closing phase was strongly dependent either on the slope of the flow rate descent or on the minimum value of the curve (regurgitation).

Figures 13 and 14 illustrate in detail the behaviour of the leaflets during the opening and closing phases, and their dynamics is compared with the case without

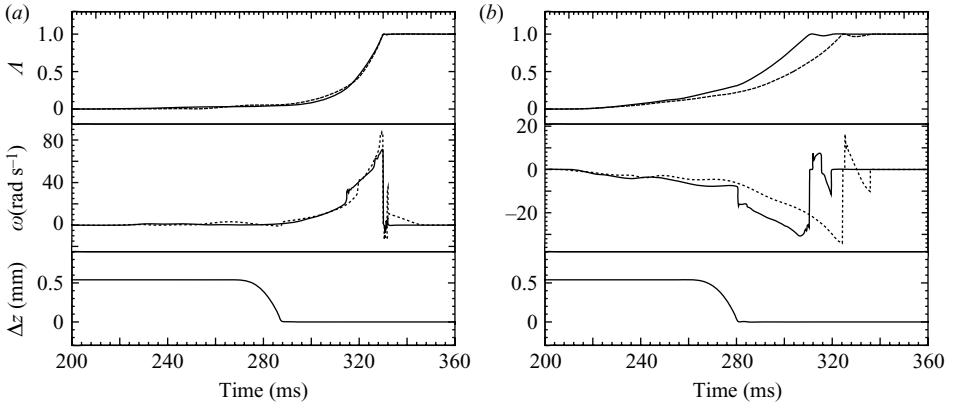

FIGURE 14. Closing phase: time variation (in ms) of the phase-averaged leaflets' angular position $\Lambda = (\alpha_{open} - \alpha)/(\alpha_{open} - \alpha_{closed})$ (top), angular velocity (middle) and axial displacement (bottom). (*a*) Leaflet 1, (*b*) leaflet 2. (———) valve with axial displacement and (·····) without axial displacement.

axial translation. The opening begins with a fast acceleration of the leaflets that reaches the maximum of the angular velocity after only one-third of the total opening time (figure 13). If axial translation is allowed, the leaflets start moving forward without appreciable rotation until they hit the hinge constraint, the angular velocity abruptly rises and a maximum is attained that exceeds the value without translation. As the valve opens, the leaflets rotate to align with the axial flow and their local linear velocity tends to become orthogonal to the main stream; as a consequence, the fluid–structure interaction produces a resistant moment that decreases the angular velocity. In the meanwhile, the mean flow velocity keeps on increasing and before reaching the fully open position, there is again a change in the acceleration sign that remains positive until the leaflets are stopped by the constraints. The closing phase, on the other hand, follows a different dynamics: It starts with small angular velocities that constantly increase, reach higher values than in the opening phase and keep accelerating until the leaflets hit the housing and reach the fully closed position. Again, the axial movement influences the leaflet angular velocity leading to a noticeably different behaviour especially for one of the leaflets, anticipating the time of closure.

A comparison of figures 13 and 14 shows that the end of the opening occurs with small angular velocities, while at the end of the closing the angular velocity attains the peak value, thus implying that in the latter case the modelling of the rebound of the leaflets at the housing might be of some relevance. Indeed, following Cheng *et al.* (2004), we have performed several preliminary simulations using a *restitution* coefficient of 0.5 which gave the angular velocity after the rebound $\omega_a = -\omega_b/2$ with ω_b the angular velocity just before the rebound. This approximation leads to a leaflet–housing interaction as a sequence of damped rebounds until the kinetic energy of the leaflet decreases to a negligible level, however its accurate time description required very small time steps that significantly added to the cost of the simulation. In addition, in some cases a 'resonance' phenomenon between the leaflets was observed, which produced high-frequency oscillations about the fully closed position. Although the consequent angular displacements were below 0.1°, resolving those oscillations required very small time steps even in the range $0.5T \leqslant t \leqslant T$, where the absence of a mean flow and the essentially steady geometrical configuration would allow a more

efficient temporal integration. We therefore set the restitution coefficient to zero. We should note that although this choice does not affect the overall leaflet dynamics, it could make a big difference if one is interested in noise production or cavitation generated in the final part of the closing phase.

3.3. *General flow features*

Instantaneous streamwise velocity contours and phase-averaged velocity profiles at different sections downstream of the valve in the planes AA and BB are reported in figures 15 and 16, respectively, for some representative times during the pulsatile cycle. At the beginning of the cycle (SO) the flow is essentially stagnant owing to the absence of mean flow for more than half period of the preceding cycle that has allowed the turbulence to settle down; the residual vortical structures however are rapidly washed away by the incoming flow as the flow rate increases. During the early opening phase the leaflets translate axially and start rotating to form a time-varying three-orifice configuration with strong shear layers shed from the valve housing, and the tips of the leaflets as shown by the panels SO and EO of figures 15 and 16. After the leaflets reach the fully open position, the flow rate keeps increasing up to the peak value (FP), thus strengthening the shear layers that become unstable. The bulk of the flow however is still laminar owing to the flow acceleration that prevents turbulence from developing. At this stage the recirculations within the Valsalva sinuses have the maximum intensity, and the mean flow downstream of the valve has the distinctive three-jet signature. Though essentially laminar, the shear layers released from the leaflets have a strong flapping motion that further enhances the flow unsteadiness. This is especially true for the upper leaflet whose wake interacts with the recirculation in the sinus of Valsalva and starts a small-scale production leading to turbulence when the flow rate decreases and an adverse pressure gradient starts to develop. The valve starts closing when the flow rate is just above one-half of the peak value, and the instantaneous as well as the mean flow are asymmetric in the two leaflets. This asymmetry is reflected also by the pressure field which causes the lower leaflet to close before the other. As the flow rate also keeps decreasing, the upper leaflet closes and the fully closed position is attained at the negative peak of the flow rate. In this configuration, most of the flow leaks through the small gaps that mimic the washing of the hinges, although we should keep in mind that the leaflets are stopped 2° before the complete closing and some minor leakage occurs also from the gaps between the leaflets and between each leaflet and the valve housing. After this phase the turbulence in the bulk starts decaying owing to the absence of forcing provided by the mean flow and the decay continues up to the beginning of a new cycle. The overall behaviour discussed above is in agreement with the computations by Dasi *et al.* (2007) and Borazjani *et al.* (2008), despite the geometrical differences of the heart valve and the aortic root.

It is important to note that the closing of the valve starts during the diastolic part of the cycle when the flow rate decreases although it is still positive ($t \geqslant 250$ ms in figure 3*b*). Due to the fact that the flow is pulsatile, it is possible to have a forward flow in the bulk of the aortic duct with a backward current close to the wall that induces strong retrograde jets within the Valsalva sinuses (figure 17); these jets are known to be responsible for the flow in the coronary arteries that depart from two of the sinuses and that might be substantially altered by the replacement of the valve. The evaluation of the persistence and strength of these jets, depending on the geometry of the remodelled aortic root as well as the position and the orientation of the replaced valve, is an important information that would be particularly helpful in

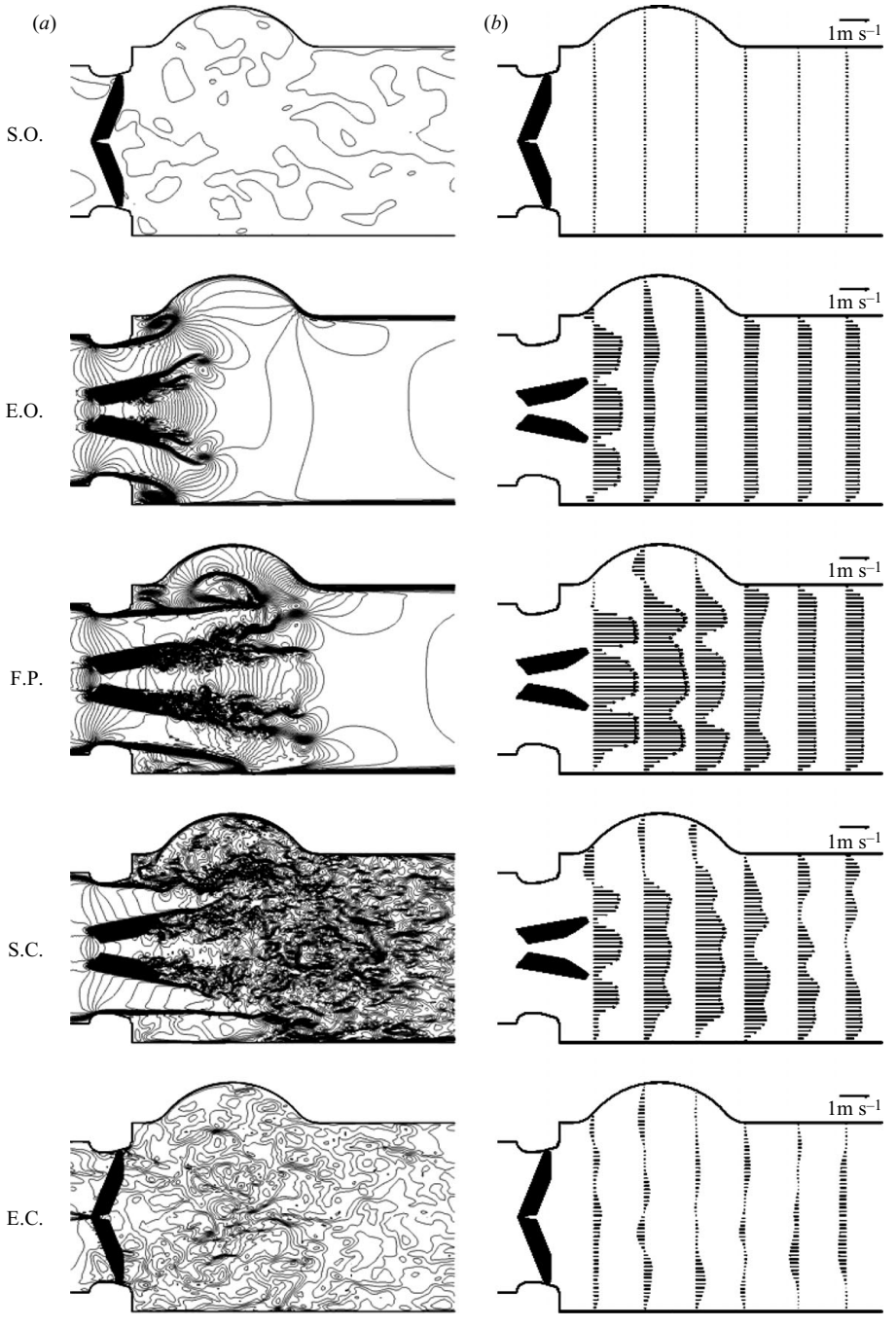

FIGURE 15. Numerical results in the plane AA: (*a*) instantaneous streamwise velocity contours; ($min = -0.8\,\mathrm{m\,s^{-1}}$, $max = 1.8\,\mathrm{m\,s^{-1}}$, $\Delta = 0.05\,\mathrm{m\,s^{-1}}$); (*b*) phase-averaged streamwise velocity profiles. (SO: start opening; EO: end opening; FP: flow rate peak; SC: start closing; EC: end closing).

surgery and could be easily obtained by numerical simulations. Another important point is that, as already mentioned, the valve is fully closed at the negative peak of the flow rate ($t \simeq 330$ ms in figure 3*b*), therefore only beyond this time a realvalve leakage

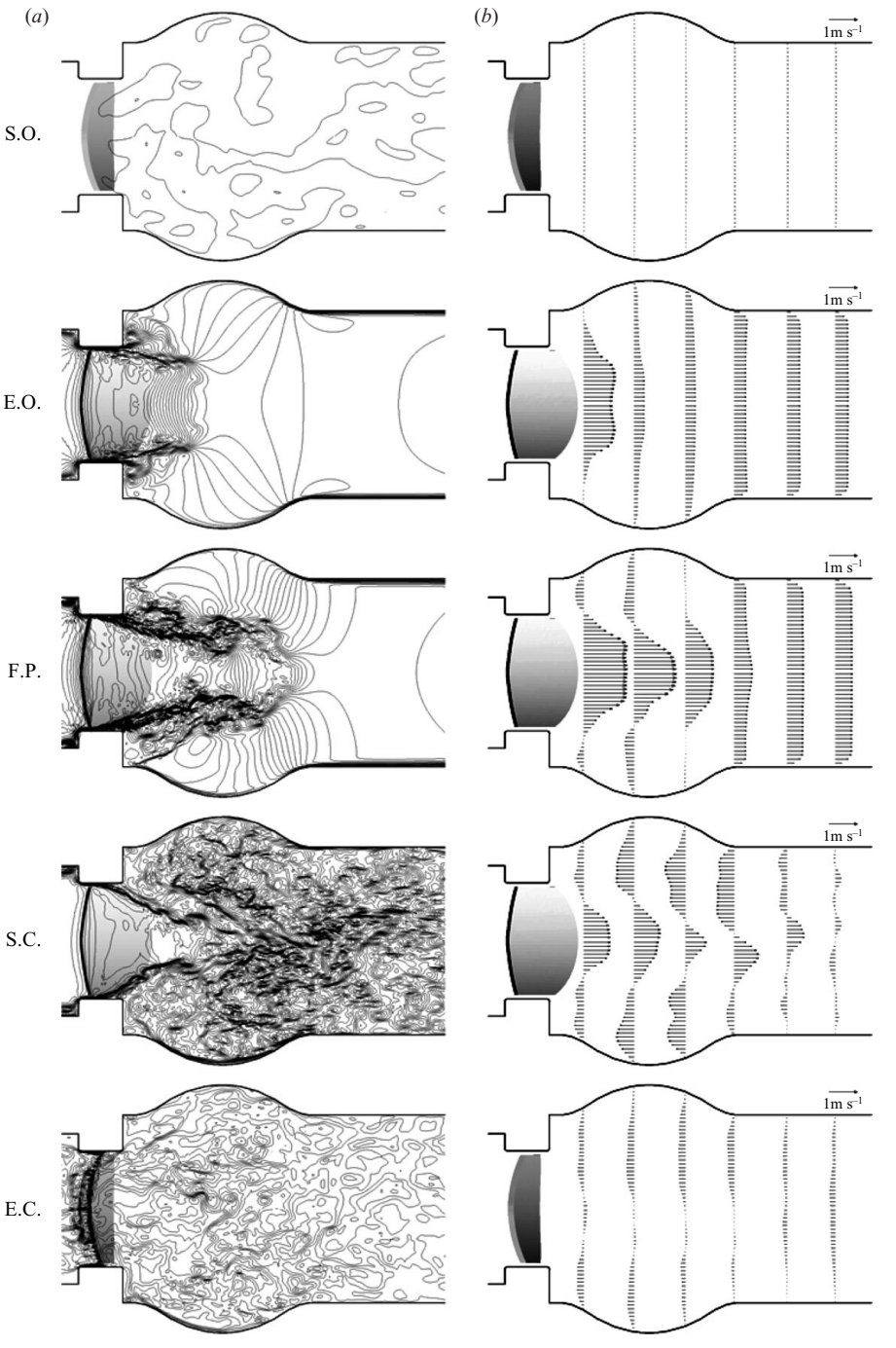

FIGURE 16. Numerical results in the centreplane BB: (*a*) instantaneous streamwise velocity contours ($min = -0.8$ m s^{-1}, $max = 1.8$ m s^{-1}, $\Delta = 0.05$ m s^{-1}); (*b*) phase–averaged streamwise velocity profiles. (SO: start opening; EO: end opening; FP: flow rate peak; SC: start closing; EC: end closing).

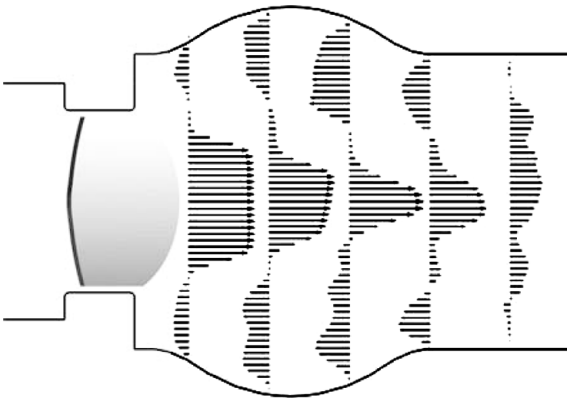

FIGURE 17. Instantaneous streamwise velocity vector snapshot in the section BB at $t \simeq 280$ ms of the cycle showing the backward jets in the Valsalva sinuses.

occurs. The negative flow rate before the closing of the valve is instead related to the retrograde rotation of the leaflets and it is often referred to as 'false regurgitation' (G. Pedrizzetti, personal communication).

As a further validation, we have computed the mean systolic pressure difference as the time-averaged pressure jump across the valve during the systolic part of the cycle ($0 \leqslant t \leqslant 300$ ms); in our simulations, for a mean flow rate of 5 l min^{-1} we have found a value of about 220 Pa corresponding to 1.6 mmHg which agrees well with the values reported by Sorin-Group (2006) in the range 1.2–1.8 mmHg, respectively for a flow rate 4.5–6.5 l min^{-1}.

3.4. *Identification of peak stresses*

In this section, we wish to illustrate another aspect of the problem in which the developed numerical tool can be efficiently employed to provide useful information. As mentioned in the introduction, high levels of stress are responsible for haemolysis and platelet activation. The haemodynamics compliance of the prosthetic heart valves is usually assessed by performing *in vitro* experiments, where two-component velocity data in significant planes, such as AA and BB of figure 2, are measured and the in-plane turbulent stresses are computed. However, as discussed in Fontaine *et al.* (1996), the flow field can vary from locally two-dimensional to completely three-dimensional with complex structures and, since the peak Reynolds stress is not invariant under coordinate system rotation (Hinze 1975), the two-dimensional analysis can underestimate the normal and shear stresses, depending on the valve model and aortic root geometry. Numerical simulations, in this respect, can complement the experiments and provide fully three-dimensional detailed information and statistics through a complete map of the regions of high stresses. Following Popov (1976), the turbulent stress analysis requires the evaluation of the full Reynolds stress tensor (that is real valued and symmetric) for every point. It is well known that in the principal coordinate system, the Reynolds stress tensor can be expressed in diagonal form with the three principal normal stresses σ_1, σ_2 and σ_3 on the diagonal, ordered usually as $\sigma_1 \geqslant \sigma_2 \geqslant \sigma_3$. The determination of the principal normal stresses involves the solution of a third-order polynomial equation of the form

$$\sigma^3 - l_1\sigma^2 + l_2\sigma - l_3 = 0, \tag{3.1}$$

where l_1, l_2 and l_3 are the three stress invariants of the tensor

$$l_1 = \overline{u'u'} + \overline{v'v'} + \overline{w'w'}, \tag{3.2}$$

$$l_2 = \overline{u'u'} * \overline{v'v'} + \overline{v'v'} * \overline{w'w'} - \overline{u'v'}^2 - \overline{v'w'}^2 - \overline{u'w'}^2, \tag{3.3}$$

l_3 is the determinant of the Reynolds stress tensor, and u', v' and w' are the fluctuations in velocity vector components in the three Cartesian directions. The principal shear stresses, aligned with planes that bisect the principal normal stress directions, are given by the following equation:

$$\sigma_{ij} = \frac{\sigma_i - \sigma_j}{2}, \qquad i, j = 1, 2, 3, \tag{3.4}$$

and then the maximum turbulent shear stress acting on a surface element is (Malvern 1977)

$$TSS^{3D}_{max} = \sigma_{13} = \frac{\sigma_1 - \sigma_3}{2}. \tag{3.5}$$

If only two-dimensional measurements are available, the same approach can be followed considering a two-dimensional space. In this case, (3.1) reduces to a second-order polynomial equation and the maximum shear stress is

$$TSS^{2D}_{max} = \frac{\sigma_1 - \sigma_2}{2} = \sqrt{\left(\frac{\overline{u'u'} - \overline{v'v'}}{2}\right)^2 + \overline{u'v'}^2}. \tag{3.6}$$

If the flow field shows one dominant velocity component, with the other two components negligible, the two-dimensional analysis can give similar results with respect to the three-dimensional one. In our case, however, the curvature of the leaflets combined with the asymmetric mounting scheme generates a complex three-dimensional flow, with the three-velocity components having comparable magnitude; the use of a two-dimensional analysis can therefore underpredict the maximum shear stresses locally. In investigating this conjecture, both two-dimensional and three-dimensional analyses are conducted near the maximum flow rate (FP), when, as shown by Woo & Yoganathan (1985), the largest measured Reynolds stresses occur. The turbulent stresses are defined by phase averages over all the computed cycles. Figure 18 shows the TSS_{max} maps for two-dimensional and three-dimensional cases, in the planes AA and BB, while figure 19 shows TSS_{max} profiles in a representative section at a distance equal to 16.0 mm from the fully open leaflet tip in the same planes (corresponding to the centre of the Valsalva sinuses). Comparing figures 18 and 19, it is evident that although the two-dimensional analysis reasonably captures the regions of high shear stress, it underpredicts the peaks severely (47 % and 45 %, respectively in planes AA and BB). This is especially true when the flow expands into the three sinus cavities, creating complex three-dimensional structures.

It should be noted that turbulent stresses, which are convective accelerations, are in fact only part of the solicitation on a fluid particle, the other part being the viscous stresses. The former are usually dominant in the bulk of the flow, but the latter prevail close to solid surfaces. It should also be mentioned that, in the bulk, viscous and turbulent stresses act on different length scales, namely in the dissipative and inertial ranges of the turbulent spectrum, respectively. At the present Reynolds number ($Re = 7200$) with a main length scale of $d = 27$ mm, we can expect a Kolmogorov dissipative scale $\eta \approx 35\,\mu$m and a dissipative range extending up to lengths of ≈ 2 mm (Pope 2000). On the other hand the turbulent shear stresses are known to be relevant mainly in the inertial range with a spectrum that decays with the wavenumbers more

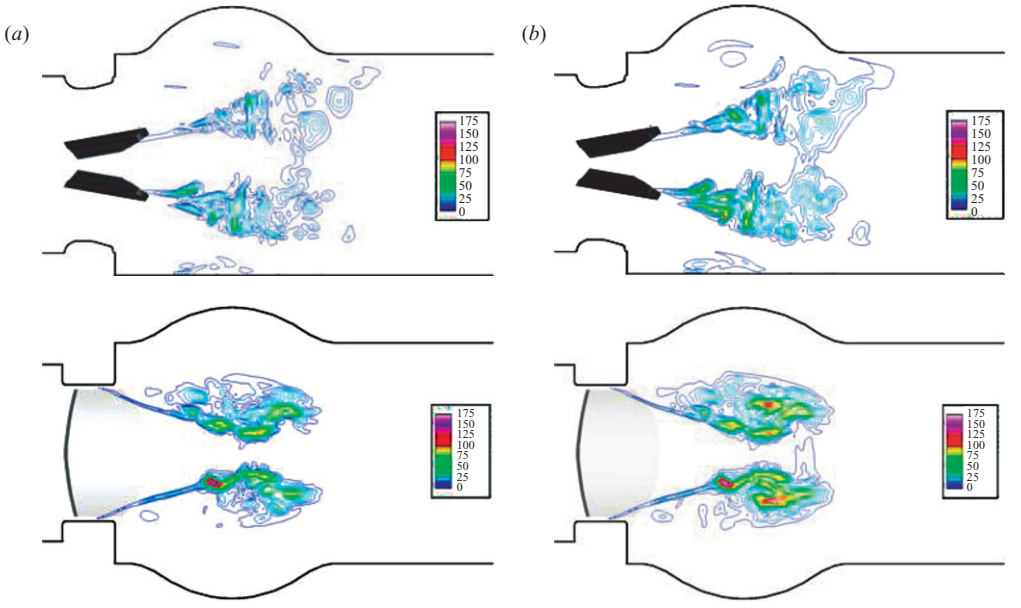

FIGURE 18. Comparison of the computed maximum value of the turbulence shear stress (in $N\,m^{-2}$) in the symmetry plane AA and in the centreplane orthogonal to the symmetry plane BB at peak of flow rate. (*a*) Two-dimensional analysis; (*b*) three-dimensional analysis.

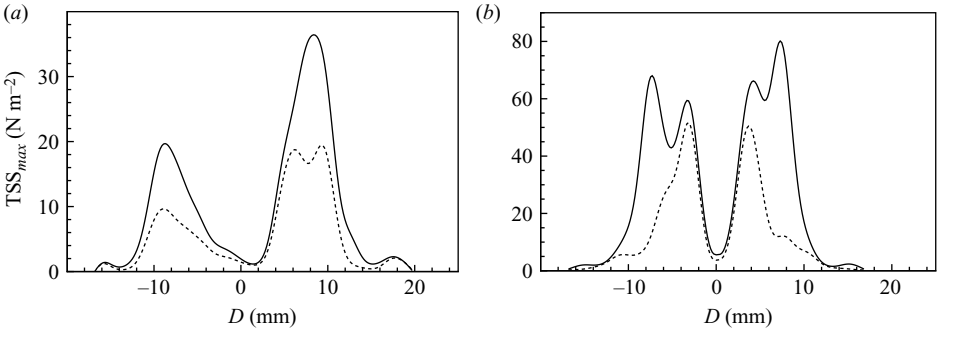

FIGURE 19. Comparison of the computed maximum value of the turbulence shear stress profiles in ($N\,m^{-2}$) at a distance equal to 16.0 mm from the fully open leaflets' tip at peak of flow rate. (*a*) Plane AA; (*b*) plane BB. ——— three-dimensional analysis; – – – – two-dimensional analysis.

rapidly than the energy spectrum. Within this scenario, since red blood cells have a diameter of about 8 μm and they are damaged by eddies of comparable size (Liu *et al.* 2000), it is possible that viscous stresses, even if smaller in magnitude, are more dangerous for haemolysis than the turbulent ones.† This consideration leads us to also examine the viscous stresses to understand what is their magnitude compared to the turbulent counterpart, and which regions of the flow are more dangerous for

† The same considerations would also hold in the case that, as suggested by Pope (2000), the Kolmogorov scale underestimates the actual size of the smallest length by more than a factor of 2, and that the dissipation spectrum peaks at about 10η.

the blood integrity. A similar study has been already conducted by Ge *et al.* (2008), where the spatial distribution of the Reynolds and viscous stresses was computed for a mechanical heart valve in an axisymmetric aortic root configuration. It should be noted, however, that the zonal assessment of stresses gives a characterization of the flow field only in terms of spots of potential blood cell damage, but the lack of information on exposure times to stresses is a major drawback. In fact, the mechanism of blood cell damage depends not only on the level of stress, but also on the exposure time to it. A Lagrangian approach is then required, with the viscous shear stress and exposure time along the trajectory that can be determined for single particles. Considering that blood fluid particles are advected by the flow and that the haemolysis depends on the history of the mechanical stresses experienced by the cells, it seems obvious that a Lagrangian analysis is needed to study this phenomenon. Nevertheless, the false notion that loads computed on Eulerian grids (often Reynolds stresses) are adequate to assess the potential risk for haemolysis has been dominating for decades, even on the specialized literature; we believe, therefore, that an explicit discussion of the above concepts is necessary.

To further stress this point, before applying the Lagrangian analysis to the complex heart valve problem, let us consider a simple model flow with a smooth two-dimensional unsteady divergence-free velocity field $u_x = A\sin(\omega t)\sin(kx)\cos(ky)$ and $u_y = -A\sin(\omega t)\sin(ky)\cos(kx)$ with A an arbitrary amplitude, $\omega = 2\pi/T$, $k = 2\pi/L$, T and L, respectively, the time and spatial periods of the flow. By time averaging over an integer number of periods T the mean components would be $\overline{u_x} = \overline{u_y} = 0$ and the velocity fluctuations are $u'_x = u_x - \overline{u_x} \equiv u_x$ and $u'_y = u_y - \overline{u_y} \equiv u_y$: the quantity TSS^{2D}_{max} can therefore be easily computed from the Reynolds stress tensor as

$$TSS^{2D}_{max} = \frac{A^2}{4}\left(\frac{[\cos(2ky) - \cos(2kx)]^2}{2} + \frac{\sin^2(2kx)\sin^2(2ky)}{4}\right)^{1/2}. \tag{3.7}$$

On the other hand, from the velocity field the rate of strain tensor can be computed from which the viscous stress tensor and its scalar equivalent τ_{eq} (see (3.9) and related discussion below) are derived

$$\tau_{eq} = \frac{2\mu k A}{3}\sin(\omega t)\cos(kx)\cos(ky), \tag{3.8}$$

with μ the dynamic viscosity of the fluid. Assuming, as commonly done in blood damage studies, that (3.7) and (3.8) represent, respectively, the turbulent and viscous stress effects on the fluid particles, there are evident differences; the two quantities have a different spatial structure with the viscous effects acting on smaller scales. The turbulent stresses, in addition, completely miss the flow time dependence and this is an important point, since the blood damage is due to an accumulation of mechanical stresses that are instantaneously experienced by the cells along their trajectory. These trajectories can be easily integrated numerically and it can be observed that some particles cross high-turbulent-stress regions with high velocity, thus accumulating a small dose of damage, while others persistently reside in a high-turbulent-stress zone but during a period in which the velocity is vanishing, without damage accumulation.

From the above discussion it is evident that turbulent stresses are, by definition, unable to account for instantaneous events that instead are the most relevant for haemolysis. In other words, the effect of the Reynolds stresses cannot be accounted on a particle trajectory of an unsteady flow because the turbulent stresses describe an averaged picture of the flow, while a particle on its trajectory is only affected by the local and instantaneous features of the field.

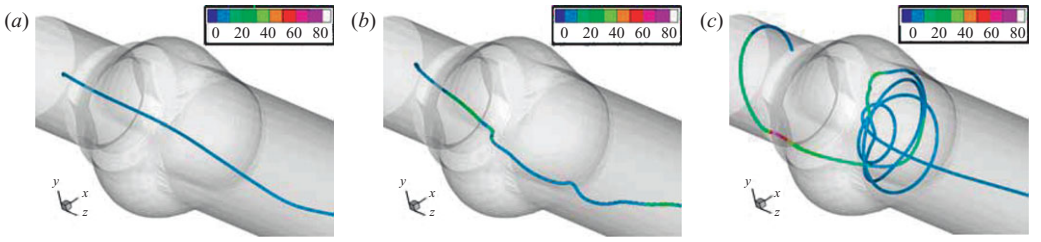

FIGURE 20. Representative particle trajectories for different initial positions. The lines are coloured by the equivalent scalar stress τ_{eq} (in $\mathrm{N\,m^{-2}}$) defined in (3.9).

The Lagrangian analysis could be easily implemented in the present numerical procedure by tracking passive particles and interpolating along the trajectory all the needed quantities. It is worth mentioning that our implementation of the Lagrangian tracking is quite general being possible to consider particles with density different from the fluid, and therefore to account for the Stokes drag, lift, added mass and other effects. Nevertheless, in this analysis we have decided to track only passive ideal particles whose trajectory $\boldsymbol{x}(t)$ is determined by $\dot{\boldsymbol{x}} = \boldsymbol{u}$, $\boldsymbol{u}$ being the fluid velocity. The reason for this choice is that our 'ideal particles' are meant to follow the trajectory of a small volume of blood still considered as a single fluid. On the other hand, tracking a single blood cell would be beyond the present computing capabilities, since in the blood the concentration of the solid part with respect to the liquid (serum) is 40 %–50 % (haematocrit), and neglecting the particle–particle interactions as well as the back reaction of the particles on the fluid would be impossible. In addition, blood cells are highly deformable, and this is the reason for the non-Newtonian behaviour of the blood in small capillaries, thus further complicating the tracking of single cells. In our analysis, we have tracked 101 particles in each flow cycle and figure 20 reports three selected trajectories showing typical behaviours; of course, each trajectory is representative of a large amount of them including cases in which a mixing of the three different dynamics is present. Note that the leaflets are not displayed because the integration of the trajectories is performed over one or more pulsating cycles, and the leaflets assume all the angular orientations between 10° and 70°. We wish to point out that the tracking of 101 particles would be certainly not enough if the computation of Lagrangian statistics had to be performed. This kind of analysis, however, would be necessary if some tracers (like micro bubbles for diagnostics) or drugs were released only from a small spot, for example a catheter, upstream of the valve and the probability for a particle to cross one particular region of the valve had to be computed. In contrast, in large vessels the blood has a spatially homogeneous composition, therefore each region of the valve is crossed by the same type of fluid particles. In addition, considering that the total volume of blood in an adult human is $\sim$5 l, the mean flow rate through the valve is 5 $\mathrm{l\,min^{-1}}$ and that the half-lifetime for red cells (the time needed for an initial population of M red cells to decrease to $M/2$) is 120 days, we can estimate an average of about 1.73×10^5 valve crossings for each fluid particle (and the red cells contained therein). On account of these numbers, it is reasonable to believe that any fluid particle will pass through all the regions of the heart valve, and that every phenomenon observed on a particular trajectory will occur many times to each fluid particle.

The effect of the viscous solicitation has been computed by the full viscous stress tensor which has been interpolated over the particle trajectory; the reduction from a

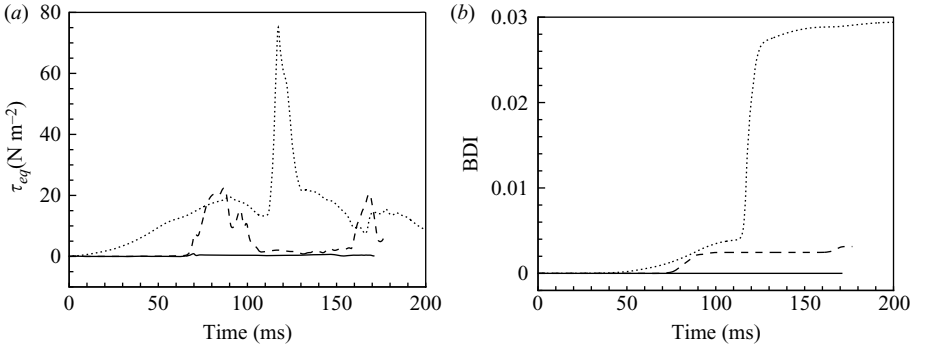

FIGURE 21. (*a*) Time evolution of the scalar equivalent stress τ_{eq} (*a*) and of the BDI (*b*) for the three trajectories of figure 6. ——— trajectory in figure 6(*a*), – – – – trajectory in figure 6(*b*) and ····· trajectory in figure 6(*c*).

second-order tensor to a single scalar quantity has been performed according to the von Mises criterion used also by Apel *et al.* (2001). This approach is useful to relate the three-dimensional stress tensor of a general flow field to a single stress value generated in a one-dimensional shear flow experimental device. In this criterion, the strains due to shear cause damage while those related to volumetric changes (that for incompressible flows are zero) are neglected. The equivalent scalar stress τ_{eq} is then obtained by equating the deformation work of a fluid element in a plain shear flow with the same work for a full three-dimensional deformation, thus yielding†

$$\tau_{eq} = \tfrac{1}{\sqrt{3}}\sqrt{\tau_{11}^2 + \tau_{22}^2 + \tau_{33}^2 - \tau_{11}\tau_{22} - \tau_{22}\tau_{33} - \tau_{11}\tau_{33} + 3\left(\tau_{12}^2 + \tau_{23}^2 + \tau_{13}^2\right)}, \qquad (3.9)$$

by which are coloured the trajectories of figure 6(*a–c*). The particles like that of figure 6(*a*) reside in the high-speed regions of the flow, far from solid walls, and typically cross the computational domain in a fraction of the heart beat. For these particles viscous stresses are negligible (figure 21*a*). Another class of particles, like in figure 6(*b*), during the motion sweeps the surface of the leaflets or of the aortic wall, and in this case the viscous stresses become non-negligible. Finally, those particles as in figure 6(*c*) crossing the tiny gaps between the leaflets and the valve housing experience very high levels of viscous stresses that are likely to produce haemolysis as is confirmed by the experience. It is worth noting that the particle in figure 6(*c*) is subject to the highest solicitation when passing through the gap mimicking the real hinge. As already mentioned, in our case the gap size is 340 μm which is bigger than that of real valves (Fallon *et al.* 2007), in addition the hinge mechanism is considerably more complex than our computational simplification, it is therefore plausible that the stress in a real valve would be even higher and consequently more dangerous for the haemolysis. As an aside, we note that considering the small physical size of the hinge gaps it could be argued that the non-Newtonian nature of the blood becomes important. There is however a two-fold reason for maintaining the Newtonian constitutive relation (i) the size of the smallest hinge gap is ∼100 μm which is still considerably bigger than the diameter of a red cell 8 μm, and (ii) the

† Following Apel *et al.* (2001), the one-dimensional work can be written as $W_{1D} = \tau_{eq}^2/(2G)$, while for the general three-dimensional expression, we have $W_{3D} = \sum_{ij}[(\tau_{ii} - \tau_{jj})^2 + 6\tau_{ij}^2]/(12G)$ with $i, j = 1, 2, 3$, τ_{ij} the generic element of the stress tensor and G the shear modulus of the material (or modulus of rigidity) whose specific value is uninfluential.

shear stresses in the gaps are the highest of all the flows, therefore the formation of rouleaux in that region is very unlikely.

To further emphasize the potential risk of haemolysis for the flow through the hinges, we can compute the percentage of the total flow rate crossing the gap regions: it is $\sim 4\,\%$ of the mean flow rate when the mean velocity is in the positive z direction (forward flow) and $\sim 7\,\%$ when the valve is closed (backward flow) for a total flow rate of $0.55\ \mathrm{l\,min^{-1}}$. Of course, these values are strongly dependent on the gap size and the particular hinge mechanism, and therefore might change considerably from valve to valve. Nevertheless, Fallon *et al.* (2007) report a range of leakage flow rates in the range 0.13–$0.69\ \mathrm{l\,min^{-1}}$ for different valve models, which is consistent with our finding. If we consider again that the half-lifetime of the red cells is 120 days, we can easily conclude that independent of the particular valve model the crossing of the hinge region is practically unavoidable for every red cell.

The modelling of the concentration of haemoglobin released (Hb) by damaged red blood cells depends on the shear stress τ and on the exposure time t through the general expression (Blackshear, Dorman & Steinbach 1965; Giersiepen *et al.* 1990),

$$I(\%) = \left(\frac{\Delta Hb}{Hb}\right)(\%) = Ct^a\tau^b, \tag{3.10}$$

where C, a and b are constants to be determined experimentally. Equation (3.10) has been extrapolated from experimental data obtained in uniform shear stress, and it must therefore be extended to a condition in which the blood is exposed to strongly time-dependent conditions. Following Blackshear *et al.* (1965), this can be achieved by introducing the *mechanical dose* $D = t\tau^{b/a}$, inspired from aims and methods of dosimetry, according to which the blood damage index (BDI) can be written as $\mathrm{BDI} = CD^a$. Assuming that during the time interval $\mathrm{d}t$ the shear stress τ remains constant, we have $\mathrm{d}D = \tau^{b/a}\mathrm{d}t$ and $\mathrm{d(BDI)} = Ca D^{a-1}\mathrm{d}D$. Omitting the mathematical details (that can be found in Grigioni *et al.* 2005), the BDI can be numerically computed by adding up the basic mechanical dose values acting on a fluid particle moving along a trajectory, resulting in the following expression:

$$\mathrm{BDI} = \sum_{i=1}^{N} Ca\left[\sum_{j=1}^{i}\tau(t_j)^{b/a}\Delta t_j + D(t_0)\right]^{a-1}\tau(t_i)^{b/a}\Delta t_i, \tag{3.11}$$

with $\Delta t_i = t_i - t_{i-1}$ the discrete time interval in which the shear stress is $\tau(t_i)$, N the number of observation time intervals along the fluid trajectory and t_0 the starting observation time. The values of parameters a, b and C are the ones originally proposed by Giersiepen *et al.* (1990), the most popular choice for the classification of haemolytic potential of artificial organs: $a = 0.785$, $b = 2.416$ and $C = 3.62 \times 10^{-5}$, if the quantities in the equation have units: s for time and $\mathrm{N\,m^{-2}}$ for the shear stresses.

The time evolution of the BDI for the three trajectories reported in figure 6 is shown in figure 21(b) where the combined effects of shear stress and exposure time can be appreciated. In particular, it is evident that the damage to a blood particle sweeping a solid surface is two-fold; not only the viscous shear stress is high, but also the velocity is reduced owing to boundary layer effects and the exposure time is long, thus increasing the damage.

Before concluding this section, we wish to stress that we do not have a comparison between viscous and turbulent stresses on a particle trajectory, since we have not found an obvious way to compute a phase-averaged quantity (turbulent Reynolds stresses) over an instantaneous Lagrangian trajectory of a fluid particle. Nevertheless,

considering the widths of the TSS_{max} peaks in figure 5 and the velocities if the FP phase of the cycle (1–1.5 m s^{-1}), the time taken by a particle to flow through these regions is smaller or comparable to the exposure time to high levels of viscous stresses (figure 21*a*). We note also that the comparison of figures 5, 6 and 21(*a*) suggests that viscous and turbulent stresses have comparable maxima but acting in different flow regions. Therefore, even if the previous discussion on turbulent, viscous stresses and related length scales is not considered, none of the stresses would be *a priori* negligible, since their effect on the blood would depend on the particular trajectory of the fluid element.

4. Conclusions

In this work, we have developed a numerical tool for studying the pulsatile flow in a mechanical heart valve with a realistic geometry of the aortic root so as to reproduce, as close as possible, an existing experiment. This has been achieved by combining the immersed boundary method with a fluid–structure interaction algorithm that proved to be accurate and efficient. The main aim was to simulate the complete dynamics of the mechanical valve without any compromise, either on the geometry of the system or on the flow physics. The results have been validated by a comparison with experimental data obtained for a similar configuration (Cerroni 2006; Romano 2008); both the leaflets dynamics and the velocity fields are in satisfactory agreement, thus confirming the reliability of the numerical data. The main bottom line of the numerical method is its inexpensiveness; first of all this technique does not need a body conformal mesh that, on account of the complex geometry with parts in relative motion, would imply a considerable computational overhead. In addition, the flow solver largely benefits from solutions on simple grids; the present simulation, in fact, could be carried out on a grid of about 6.6 million nodes using about 1.6×10^4 time steps per heart cycle within 1 Gb of RAM memory on a 3 GHz P-IV single processor in about 60 h per cycle.

In addition to the basic features, the systematic delay in the closing of one of the leaflets and the effect of their axial translation have been investigated in detail. It has been observed that the asymmetric valve mounting with respect to the Valsalva sinuses causes one of the leaflets (the upper half in figure 3*a*) to face directly one sinus; the recirculation in the latter during the diastole produces a low-pressure distribution on the outer leaflet's surface that delays its closing with respect to the other leaflet. It is known that the recirculation areas within the sinuses throughout the aortic root during the diastolic phase have a fundamental role in the feeding of the coronary arteries that depart from two of the sinuses. While these recirculation areas have been observed to persist also in presence of a mechanical valve (figure 17), it is not clear how the valve position/orientation and the remodelling of the aortic root after the valve replacement alter the coronary flow. This is a fundamental point, because in a valve implantation it is presently difficult to preserve the anatomical shape of the aortic root and the latter is sometimes reduced to a much simpler shape for the sake or durability and reliability of the intervention (Bental procedure). All these points are being investigated and they will be the subject of a dedicated study.

Since the main drawback of the mechanical heart valves is the propensity to haemolysis and platelet activation, we have also investigated the production and spatial distribution of shear stresses in the flow field. We have found that viscous and turbulent stresses have comparable magnitude, although in different flow regions, and therefore none of them is *a priori* negligible. Nevertheless, considerations on the

red cell dimensions, the Kolmogorov scale and the turbulent shear stress spectrum suggest that viscous stresses are potentially more dangerous, since they act on length scales comparable to that of the blood cells. This is indirectly confirmed by the experimental observations, showing that most of haemolysis occurs during the end of the closing phase (Kini *et al.* 2000), owing to the squeezing of the red cells between the leaflets and the valve housing, and in the flow through the hinges. Nevertheless, platelets, responsible for clots and thrombus formation, are activated at lower levels of stress than those necessary for haemolysis; the augmented mechanical stresses generated by the mechanical valve certainly deserve more investigation and it is currently under study by comparing different valve geometries and flow conditions.

Many things could be done to extend and improve the present investigation: One of them is to increase the number of simulated flow cycles in order to get more converged statistics. We note, however, that the r.m.s. of the velocity profiles already capture the correct magnitude and peak positions with respect to the experimental data obtained by averaging over 200 cycles. Another point could be a more realistic modelling of the hinge geometry, especially on considering that the flow in that region is responsible for the highest viscous stresses and is implicated for haemolysis. Finally, the deformation of the aortic walls could change either the turbulence features or the leaflets dynamics through an alteration of the pressure gradients along the flow; this is a big difference between *in vitro* and *in vivo* investigations and numerical simulations could be very helpful in this respect.

We would like to acknowledge Professor G. P. Romano and Dr M. Falchi (University of Roma 'La Sapienza') for having kindly provided the experimental data for the comparison and for many useful discussions. The experimental data have been obtained by Professor G. P. Romano in the frame of the European Commission FP6 funded project, Smart-PIV (IST-2001-37548 contract). The paper has benefited from several discussions with Professor G. Pedrizzetti. The authors are also indebted to Mr A. Schembri Volpe for having implemented the particle tracking procedure in the code. This research has been partly supported by CEMeC (Centro d'Eccellenza di Meccanica Computazionale) of Politecnico di Bari. E. Balaras and A. Cristallo were partially supported by the National Science Foundation (Grant CTS-0347011).

REFERENCES

Alemu, Y. & Bluestein, D. 2007 Flow-induced platelet activation and damage accumulation in a mechanical heart valve: numerical studies. *Artif. Organs* **31** (9), 677–688.

Apel, J., Reinhard, P., Klaus, S., Siess, T. & Reul, H. 2001 Assessment of hemolysis related quantities in a microaxial blood pump by computational fluid dynamics. *Artif. Organs* **25** (5), 341–347.

Blackshear, P. L., Dorman, F. D. & Steinbach J. H. 1965 Some mechanical effects that influence hemolysis. *Trans. Am. Soc. Artif. Intern. Organs* **11**, 112–118.

Borazjani, I., Ge, L., Dasi, P. L., Sotiropoulos, F. & Yoganathan, A. P. 7–8 June 2007 Fluid-structure interaction in bi-leaflet mechanical heart valves. In *2nd Frontier in Biomedical Devices Conference*, California, USA, BioMed 2007-3807.

Borazjani, I., Ge, L. & Sotiropulos, F. 2008 Curvilinear immersed boundary method for simulating fluid structure interaction with complex 3d rigid bodies. *J. Comput. Phys.* **227**, 7587–7620.

Brücker, C., Steinseifer, U., Schröder, W. & Reul, H. 2002 Unsteady flow through a new mechanical heart valve prosthesis analysed by digital particle image velocimetry. *Meas. Sci. Technol.* **13**, 1043–1049.

Caro, C. G., Pedley, T. J., Schroter, R. C. & Seed, W. A. 1978 *The Mechanics of the Circulation*. Oxford University Press.

Causin, P., Gerbeau, J. F. & Nobile, F. 2005 Added-mas effect in the design of partitioned algorithms for fluid-structure problems. *Comput. Methods Appl. Mech. Engng* **194**, 4506–4527.

Cerroni, G. 2006 Studio sperimentale del campo fluidodinamico a valle di una valvola cardiaca artificiale e in un dispositivo di circolazione assistita mediante tecnica PIV. Master's thesis, Universita' degli studi di Roma, La Sapienza, Facolta' di Ingegneria.

Cheng, R., Lai, Y. G. & Chandran K. B. 2004 Three-dimensional fluid-structure interaction simulation of bileaflet mechanical heart valve flow dynamics. *Ann. Biomed. Engng* **32** (13), 1471–1483.

Cristallo, A. & Verzicco, R. 2006 Combined immersed boundary/large-eddy-simulations of incompressible three dimensional complex flows. *Flow Turbul. Combust.* **77**, 3–26.

Dasi, L. P., Ge, L., Simon, H. A., Sotiropoulos, F. & Yoganathan A. P. 2007 Vorticity dynamics of a bileaflet mechanical heart valve in an axisymmetric aorta. *Phys. Fluids* **19**, 1–17.

Fadlun, E. A., Verzicco, R., Orlandi, P. & Mohd-Yosuf, J. 2000 Combined immersed-boundary finite-difference methods forthree-dimensional complex flow simulations. *J. Comput. Phys.* **161**, 35–60.

Fallon, A. M., Marzec, U. M., Hanson, S. R. & Yoganathan, A. P. 2007 Thrombin formation *in vitro* in response to shear-induced activation of platelets. *Thrombosis Res.* **121**, 397–406.

Fontaine, A. A., Ellis, J. T., Healy, T. M., Hopmeyer, J. & Yoganathan, A. P. 1996 Identification of peak stresses in cardiac prostheses. A comparison of two-dimensional versus three-dimensional principal stress analyses. *ASAIO J.* **42**, 154–163.

Ge, L., Dasi, L. P., Sotiropulos, F. & Yoganathan, A. P. 2008 Characterization of hemodynamic forces induced by mechanical heart valves: Reynolds vs. viscous stresses. *Ann. Biomech. Engng* **36**, 276–297.

Ge, L., Leo, H. L., Sotiropulos, F. & Yoganathan, A. P. 2005 Flow in a mechanical bileaflet heart valve at laminar and near-peak systole flow rates: CFD simulations and experiments. *J. Biomech. Engng* **127**, 782–797.

Giersiepen, M., Wurzinger, L. J., Opitz, R. & Reul, H. 1990 Estimation of shear stress related blood damage in heart valve prosteses: In vitro comparison of 25 aortic valves. *Intl J. Artif. Organs* **13** (5), 300–306.

Grigioni, M., Morbiducci, U., D'Avenio, G., Di Benedetto, G. & Del Gaudio, C. 2005 A novel formulation for blood trauma prediction by a modified power-law mathematical model. *Biomech. Model Mechanobiol.* **4**, 249–260.

Hinze, J. O. 1975 *Turbulence*. Mc Graw & Hill.

Iaccarino, G. & Verzicco, R. 2003 Immersedboundary technique for turbulent flow simulations. *Appl. Mech. Rev.* **56**, 331–347.

Kini, V., Bachmann, C., Fontaine, A., Deutsch, S. & Tarbell, J. M. 2000 Flow visualization in mechanical heart valves: occluder rebound and cavitation potential. *Ann. Biomed. Engng* **28**, 431–441.

Ku, D. N. & Liepsch, D. W. 1986 The effects of non-Newtonian viscoelasticity and wall elasticity on flow at 90 degrees bifurcation. *Biorheology* **23**, 359–370.

Le Tallec, P. & Mouro, J. 2001 Fluid structure interaction with large structural displacements. *Comput. Methods Appl. Mech. Engng* **190**, 3039–3067.

Liepsch, D. W. 1986 Flows in tubes and arteries: a comparison. *Biorheology* **23**, 395–433.

Liepsch, D. W., Pflugbeil, G., Matsuo, T. & Lesniak, B. 1998 Flow visualization in 1- and 3-d laser–doppler–anemometer measurements in model of human carotid arteries. *J. Clin. Hemorheol. Microcirc.* **18**, 1–30.

Liu, J. S., Lu, P. C. & Chu, S. H. 2000 Turbulence characteristics downstream of bileaflet aortic valve prostheses. *J. Biomech. Engng* **122**, 118–124.

Malvern, L. E. (1977) *Introduction to the Mechanics of a Continuous Medium.* Prentice Hall, Inc.

Myers, M. R. & Porter, J. M. 2003 Impulsive-motion model for computing the closing motion of mechanical heart-valve leaflets. *Ann. Biomed. Engng* **31**, 1031–1039.

Nichols, W. W. & O'Rourke, M. F. 1990 *McDonald's Blood Flow in Arteries*. Lea & Febiger.

Pedrizzetti, G. & Domenichini, F. 2006 Flow-driven opening of a valvular leaflet. *J. Fluid Mech.* **569**, 321–330.

Pedrizzetti, G. & Domenichini, F. 2007 Asymmetric opening of a simple bi-leaflet valve. *Phys. Rev. Lett.* **98**, 214503.

Pope, S. B. 2000 *Turbulent Flows*. Cambridge University Press.

Popov, E. P. 1976 *Mechanics of Materials,* 2nd ed. Prentice Hall Inc.

Romano, G. P. 2008 Deliverable d24-study case report n 2 pulse duplicator with aortic root model from rwth aachen smart-piv ist-2002-37548 European project. Available at http://www.smart–piv.com.

Smith, R., Blick, E., Coalson, J. & Stein, P. 1972 Thrombus production by turbulence. *J. Appl. Physiol.* **32**, 261–264.

Sorin-Group 2006 *Sorin Biomedica.* Available at http://www.sorinbiomedica.com.

Stein, P. D. & Sabbah, M. N. 1974 Measured turbulence and its effect on thrombus formation. *Circ. Res.* **35**, 608–614.

Swartzrauber, P. N. 1974 A direct method for the discrete solution of separable elliptic equations. *SIAM J. Numer. Anal.* **11**, 1136–1150.

Verzicco, R. & Orlandi, P. 1996 A finite difference scheme for three-dimensional incompressible flows in cylindrical coordinates. *J. Comput. Phys.* **123**, 402–413.

Whitmore, R. L. 1968 *Rheology of the Circulation*. Pergamon Press.

Woo, Y. R. & Yoganathan, A. P. 1985 In vitro pulsatile flow velocity and turbulent shear stress measurements in the vicinity of mechanical aortic heart valve prostheses. *Life Support Syst.* **3**, 283–312.

Yang, J. & Balaras, E. 2006 An embeddedboundary formulation for large eddy simulation of turbulent flows interacting withmoving boundaries. *J. Comput. Phys.* **215**, 12–40.

Yang, J., Preidikman, S. & Balaras, E. 2008 A strongly-coupled embedded boundary method for fluid–structure interaction of elastically mounted rigid bodies. *J. Fluids Struct.* **182**, 167–182.

Yoganathan, A. P., He, Z. & Jones, S. C. 2004 Fluid mechanics of heart valves. *Annu. Rev. Biomed. Engng* **6**, 331–362.

Yokoyama, Y., Medart, D., Hormes, M., Schmitz, C., Hamilton, K., Kwant, P. B., Takatani, S., Schmitz-Rode, T. & Steinseifer, U. 2006 CFD simulation of a novel bileaflet mechanical heart valve prosthesis – an estimation of the Venturi passage formed by the leaflets. *Intl J. Artif. Organs* **29** (12), 1132–1139.